To further clarify the abnormality in excitation–contraction coupling of the cardiomyopathic myocytes, interventions such as changing pacing rate or giving inotropic agent would be useful. However, under such interventions, cardiomyopathic myocytes became highly irritable against stretch and started spontaneous irregular contractions. Unfortunately, we do not have any measures to circumvent this problem at present.

4.4. Summary

In summary, cardiomyocytes isolated from cardiomyopathic hamsters (Bio TO-2 strain) showed impaired contractile function compared to those from normal control hamsters, and the contractile dysfunction was pronounced in the indices obtained under high load conditions. These findings indicate the importance of evaluating myocyte function under high load and also provide suggestions for the pathogenesis of this disease condition.

Acknowledgements

We thank Ms. C. Miyazawa for her excellent technical assistance. This study was supported by grants from the Program for Promotion of Fundamental Studies in Health Sciences of the Organization for Pharmaceutical Safety and Research, the Vehicle Racing Commemorative Foundation, Suzuken Memorial Foundation and the Research Grant for Cardiovascular Disease from the Ministry of Health, Labour and Welfare. K.P.Y. was supported by a Grant-in-Aid for JSPS Fellows related to a JSPS Postdoctoral Fellowship for Foreign Researchers.

References

[1] Sakamoto A, Ono K, Abe M, Jasmin G, Eki T, Murakami Y, et al. Both hypertrophic and dilated cardiomyopathies are caused by mutation of the same gene, delta-sarcoglycan, in hamster: an animal model of disrupted dystrophin-associated glycoprotein complex. Proc Natl Acad Sci USA 1997;94:13873–8.

[2] Makino N, Masutomo K, Nshimura M, Maruyama T, Yanaga T. Cardiac collagen expression in the development of two types of cardiomyopathic hamsters (Bio. 14.6 and Bio 53.58. In: Nagano M, Takeda N, Dhalla NS, editors. THe cardiomyopathic heart. New York: Raven Press; 1994. p. 1–65.

[3] Panchal BC, Trippodo NC. Systemic and regional haemodynamics in conscious BIO TO-2 cardiomyopathic hamsters. Cardiovasc Res 1993;27:2264–9.

[4] Goineau S, Pape D, Guillo P, Ramée MP, Bellissant E. Hemodynamic and histomorphometric characteristics of dilated cardiomyopathy of Syrian hamsters (Bio TO-2 strain). Can J Phsyiol Phramacol 2001;79: 329–37.

[5] Capasso JM, Olivetti G, Anversa P. Mechanical and electrical properties of cardiomyopathic hearts of Syrian hamsters. Am J Physiol 1989;257:H1836–H1842.

[6] Antony I, Chemla D, Lecarpentier Y. Myocardial contractility, lusitropy and calcium responsiveness in young (50 days) and hypertrophied (180 days) cardiomyopathic hamsters. J Mol Cell Cardiol 1992;24(10):1089–100.

[7] Hatem SN, Sham JSK, Morad M. Enhanced Na^+–Ca^{2+} exchange activity in cardiomyopathic Syrian hamster. Circ Res 1994;74:253–61.

[8] Howlett SE, Bobet J, Gordon T. Force-interval relation in normal and cardiomyopathic hamster atria. Am J Physiol 1991;261:H1597–H1602.

[9] Sen L, O'neill M, Marsh JD, Smith TW. Inotropic and calcium kinetic effects of calcium channel agonist and antagonist in isolated cardiac myocytes from cardiomyopathic hamsters. Circ Res 1990;67:599–608.

[10] Sen L, O'neill M, Marsh JD, Smith TS. Myocyte structure, function, and calcium kinetics in the cardiomyopathic hamster heart. Am J Physiol 1990;259:H1533–H1543.

[11] Rossner KL. Calcium current in congestive heart failure of hamster cardiomyopathy. Am J Physiol 1991;260:H1179–H1186.

[12] Howlett SE, Xiong W, Mapplebeck CL, Ferrier GR. Role of voltage-sensitive release mechanisms in depression of cardiac contraction in myopathic hamsters. Am J Physiol 1999;277:H1690–H1700.

[13] Yasuda S, Sugiura S, Kobayakawa N, Fujita H, Yamashita H, Katoh K, et al. A novel method to study contraction characteristics of a single cardiac myocyte using carbon fibers. Am J Physiol Heart Circ Physiol 2001;281(3):H1442–H1446.

[14] Nishimura S, Yasuda S, Katoh M, Yamada KP, Yamashita H, Saeki Y, et al. Single cell mechanics of rat cardiomyocytes under isometric, unloaded and physiologically loaded conditions. Am J Physiol 2004; 287:H196–H202.

[15] Yasuda S, Sugiura S, Yamashita H, Nishimura S, Saeki Y, Momomura S, et al. Unloaded shortening increases the peak of Ca^{2+} transients but accelerates their decay in rat single cardiac myocytes. Am J Physiol 2003;285:H470–H475.

[16] Ikenouchi H, Peters GA, Barry WH. Evidence that binding of indo-1 to cardiac myocyte protein does not markedly change K_d for Ca^{2+}. Cell Calcium 1991;12:415–22.

[17] Martin AF, Pagani ED, Solaro RJ. Thyroxine-induced redistribution of isozymes of rabbit ventricular myosin. Circ Res 1982;50:117–24.

[18] Kruger C, Erdman E, Nabauer M, Beuckelmann DJ. Intracellular calcium handling in isolated ventricular myocytes from cardiomyopathic hamsters (strain BIO 14.6) with congestive heart failure. Cell Calcium 1994;16:500–8.

[19] Sorenson AL, Tepper D, Sonnenblick EH, Robinson TF, Capasso JM. Size and shape of enzymatically isolated ventricular myocytes from rats and cardiomyopathic hamsters. Cardiovasc Res 1985;19(12): 793–9.

[20] Bluhm WF, McCulloch AD, Lew WY. Active force in rabbit ventricular myocytes. J Biomech 1995;28(9):1119–22.

[21] Palmer RE, Brady AJ, Roos KP. Mechanical measurement from isolated cardiac myocytes using a pipette attachment system. Am J Physiol 1996;270:C697–C704.

[22] Janssen PM, de Tombe PP. Uncontrolled sarcomere shortening increases intracellular Ca^{2+} transient in rat cardiac trabeculae. Am J Physiol 1997;272(4 Pt 2):H1892–H1897.

[23] Backx PH, Gao WD, Azan-Backx MD, Marban E. Mechanism of force inhibition by 2,3-butanedione monoxime in rat cardiac muscle: roles of $[Ca^{2+}]_i$ and cross-bridge kinetics. J Physiol 1994;476(3):487–500.

[24] Matsumura K, Arai K, Zhong D, Saito F, Fukuta-Ohi H, Maekawa R, et al. Disruption of dystroglycan axis by ß-dystroglycan processing in cardiomyopathic hamster muscle. Neuromuscul Disord 2003;13:796–803.

[25] Kawada T, Nakatsuru Y, Sakamoto A, Koizumi T, Shin WS, Okai-Matsuo Y, et al. Strain- and age-dependent loss of sarcoglycan complex in cardiomyopathic hamster hearts and its re-expression by d-sarcoglycan gene transfer in vivo. FEBS Lett 1999;458:405–8.

[26] Wiegand V, Stroh E, Henniges A, Lossnitzer K, Kreuzer H. Altered distribution of myosin isoenzymes in the cardiomyopathic Syrian hamster (BIO 8.262). Basic Res Cardiol 1983;78(6):665–70.

[27] Malhotra A, Karell M, Scheuer J. Multiple cardiac contractile protein abnormalities in myopathic Syrian hamsters (BIO 53: 58). J Mol Cell Cardiol 1985;17(2):95–107.

[28] Pagani ED, Julian FJ. Rabbit papillary muscle myosin isozymes and teh velocity of muscle shortening. Circ Res 1984;54:586–94.

[29] Cappelli V, Bottinelli R, Poggesi C, Moggio R, Reggiani C. Shortening velocity and myosin and myofibrillar ATPase activity related to myosin isoenzyme composition during postnatal development in rat myocardium. Circ Res 1989;65:446–57.

[30] Josephson RA, Spurgeon HA, Lakatta EG. The hyperthyroid heart. An analysis of systolic and diastolic properties in single rat ventricular myoyctes. Circ Res 1990;66:773–81.

[31] Yamashita H, Sugiura S, Serizawa T, Sugimoto T, Iizuka M, Katayama E, et al. Sliding velocity of isolated rabbit cardiac myosin correlates with isozyme distribution. Am J Physiol 1992;263:H464–H472.

[32] Yamashita H, Sugiura S, Sata M, Serizawa T, Iizuka M, Shimmen T, et al. Depressed sliding velocity of isolated cardiac myosin from cardiomyopathic hamsters: evidence for an alteration in mechanical interaction of actomyosin. Mol Cell Biochem 1993;119:79–88.

[33] VanBuren P, Harris DE, Alpert NR, Warshaw DM. Cardiac V_1 and V_3 myosins differ in their hydrolytic and mechanical activation in vitro. Circ Res 1995;77:439–44.

[34] Sugiura S, Kobayakawa N, Momomura S, Chaen S, Omata M, Sugi H. Different cardiac myosin isforms exhibit equal force-generating ability in vitro. Biochim Biophys Acta 1996;1273:73–6.

[35] de Tombe PP, Wannengurg T, Fan D, Little WC. Right ventricular contractile protein function in rats with left ventricular myocardial infarction. Am J Physiol 1996;271:H73–H79.

[36] Nigro V, Okazaki Y, Belsito A, Piluso G, Matsuda Y, Politano L, et al. Identification of the Syrian hamster cardiomyopathy gene. Hum Mol Genet 1997;6:601–7.

[37] Towbin JA, Bowels NE. The failing heart. Nature 2002;415:227–33.

[38] Granzier HL, Irving TC. Passive tension in cardiac muscle: contribution of collagen, titin, microtubules, and intermediate filaments. Biophys J 1995;68(3):1027–44.

[39] Shah SB, Su FC, Jordan K, Milner DJ, Friden J, Capetanaki Y, et al. Evidence for increased myofibrillar mobility in desmin-null mouse skeletal muscle. J Exp Biol 2002;205:321–5.

Overexpression of eNOS in brain stem reduces enhanced sympathetic drive in mice with myocardial infarction

Koji Sakai, Yoshitaka Hirooka, Hideaki Shigematsu, Takuya Kishi, Koji Ito, Hiroaki Shimokawa, Akira Takeshita and Kenji Sunagawa

AJP - Heart 289:2159-2166, 2005. First published Jul 8, 2005; doi:10.1152/ajpheart.00408.2005

Am J Physiol Heart Circ Physiol 289: H2159–H2166, 2005.
First published July 8, 2005; doi:10.1152/ajpheart.00408.2005.

Overexpression of eNOS in brain stem reduces enhanced sympathetic drive in mice with myocardial infarction

Koji Sakai, Yoshitaka Hirooka, Hideaki Shigematsu, Takuya Kishi, Koji Ito, Hiroaki Shimokawa, Akira Takeshita, and Kenji Sunagawa

Department of Cardiovascular Medicine, Kyushu University Graduate School of Medical Sciences, Fukuoka, Japan

Submitted 25 April 2005; accepted in final form 5 July 2005

Sakai, Koji, Yoshitaka Hirooka, Hideaki Shigematsu, Takuya Kishi, Koji Ito, Hiroaki Shimokawa, Akira Takeshita, and Kenji Sunagawa. Overexpression of eNOS in brain stem reduces enhanced sympathetic drive in mice with myocardial infarction. *Am J Physiol Heart Circ Physiol* 289: H2159–H2166, 2005. First published July 8, 2005; doi:10.1152/ajpheart.00408.2005.—Reduced nitric oxide (NO) in the brain might contribute to enhanced sympathetic drive in heart failure (HF). The aim of this study was to determine whether increased NO production induced by local overexpression of endothelial NO synthase (eNOS) in the nucleus tractus solitarius (NTS) of the brain stem reduces the enhanced sympathetic drive in mice with HF. Myocardial infarction (MI) was induced in mice by ligating the left coronary artery. MI mice exhibited left ventricular dilatation and a reduced left ventricular ejection fraction. Urinary norepinephrine excretion in MI mice was greater than that in sham-operated mice, indicating that sympathetic drive was enhanced in this model. Thus this model has features that are typical of HF. Western blot analysis and immunohistochemical staining for neuronal NOS (nNOS) indicated that nNOS protein expression was significantly reduced in the brain stem of MI mice. MI mice had a significantly smaller increase in blood pressure evoked by intracisternal injection of N^G-monomethyl-L-arginine than sham-operated mice. Adenoviral vectors encoding either eNOS (AdeNOS) or β-galactosidase (Adβgal) were transfected into the NTS to examine the effect of increased NO production in the NTS on the enhanced sympathetic drive in HF. After the gene transfer, urinary norepinephrine excretion was reduced in AdeNOS-transfected MI mice but not in Adβgal-transfected MI mice. These results indicate that nNOS expression in the brain stem, especially in the NTS, is reduced in the MI mouse model of HF, and increased NO production induced by overexpression of eNOS in the NTS attenuates the enhanced sympathetic drive in this model.

nitric oxide; heart failure; brain; sympathetic; genes

CHRONIC HEART FAILURE (HF) is characterized by enhanced neurohumoral drive in experimental animals as well as in patients (27, 29, 55). Sympathetic and humoral activation precede the onset of clinically recognized HF (11). In particular, there is accumulating evidence that β-blockers are one of the most effective drugs for treatment of patients with chronic HF (3, 31, 48), supporting the idea that the activation of the sympathetic nervous system has an important role in the progression of HF. In fact, plasma norepinephrine levels increase in relation to the severity of HF and correlate with mortality rates in patients with chronic HF (4, 38). The exact mechanisms underlying sympathoexcitation in HF are not clear, although several mechanisms have been proposed. Recent studies (27, 29, 55) suggest that the central nervous system (CNS) is involved in the mechanism(s) underlying sympathoexcitation in HF.

The nucleus tractus solitarius (NTS) in the brain stem is involved in regulating blood pressure, heart rate, and sympathetic nerve activity (1, 5, 23). The NTS receives inputs from afferent fibers arising from arterial baroreceptors, chemoreceptors, cardiopulmonary receptors, and other visceral receptors and thus has an important role in autonomic control of the cardiovascular system (1, 5, 23). There is considerable evidence that nitric oxide (NO) in the CNS, including the NTS, inhibits sympathetic nerve activity (14, 16, 33, 46, 52). In addition, there are high concentrations of neuronal NO synthase (nNOS) in brain stem regions, particularly in the NTS, as demonstrated by immunohistochemistry, NADPH-diaphorase staining, and autoradiography studies (7, 13, 47). Recent studies (18, 33, 50, 54) demonstrated reduced nNOS expression in the paraventricular nucleus (PVN) of the hypothalamus in a rat model of HF. Although the mRNA level of nNOS in the brain stem is reduced (33), the pathophysiological role of NO in the brain stem, particularly in the NTS, in HF is not known. Thus a more precise physiological investigation related to the NTS is necessary.

Therefore, we hypothesized that NOS in the brain stem, particularly in the NTS, is altered in HF, and this alteration contributes to the sympathoexcitation in the mouse model with HF. The aim of the present study was to determine whether endogenous nNOS in the brain stem is reduced in a mouse model of HF. Myocardial infarction (MI) was produced by left coronary artery (LCA) occlusion in mice to determine whether this model exhibits sympathoexcitation similar to that in human HF and changes in nNOS expression. Second, we transfected adenoviral vectors encoding endothelial NOS (AdeNOS) into the NTS to increase local NO production in the NTS of mice, using a technique previously established in rats (17, 22, 39). Urinary norepinephrine excretion was measured as a marker of the sympathetic nerve activity. We examined the effect of increased NO production induced by the transfection of AdeNOS in the NTS on sympathetic nerve activity.

METHODS

Animals and surgery. This study was reviewed and approved by the Committee on Ethics of Animal Experiments, Faculty of Medicine, Kyushu University, and conducted according to the *Guidelines for Animal Experiments of the Faculty of Medicine*, Kyushu University (Fukuoka, Japan). Male CD-1 mice (10 to 12 wk old, weight 30–40 g, Charles River Japan, Yokohama, Japan) underwent coronary artery

Address for reprint requests and other correspondence: Y. Hirooka, Dept. of Cardiovascular Medicine, Kyushu Univ. Graduate School of Medical Sciences, 3-1-1 Maidashi, Higashi-ku, Fukuoka 812-8582, Japan (e-mail: hyoshi@cardiol.med.kyushu-u.ac.jp).

The costs of publication of this article were defrayed in part by the payment of page charges. The article must therefore be hereby marked "*advertisement*" in accordance with 18 U.S.C. Section 1734 solely to indicate this fact.

American Journal of Physiology - Heart and Circulatory Physiology

ligation to produce MI. The surgical procedures are described in detail elsewhere (28). Briefly, after pentobarbital sodium anesthesia (25–40 mg/kg ip) and intubation with a polyethylene tube (size 60), animals were ventilated by using a volume-cycled rodent respirator with 2 to 3 ml/cycle at a respiratory rate of 120 breaths/min. After thoracotomy, the LCA was ligated with a suture, 3 to 4 mm from the tip of the left auricle. The chest wall and skin were closed with a suture. The same surgical procedures were performed in sham mice, except that the coronary artery was not ligated.

LV morphology and morphometry. Four weeks after LCA ligation, the left ventricle (LV), including the septum, and the right ventricle were dissected to confirm MI in some groups of mice. After the major long-axis intracavitary diameter was measured, each LV was serially sectioned into three rings perpendicular to the major axis of the heart, after which the short-axis diameter was measured. At the midregion, the minimal and maximal chamber diameters were used with the long-axis diameter to compute the LV chamber volume. Infarct size in these hearts was determined by the method described previously (40). Briefly, serial 5-μm sections were prepared, mounted, and stained with Masson trichrome. Infarct length was measured along the endo- and epicardial surfaces from each of the three LV sections, and values from all three sections were summed. Total LV circumference was calculated as the sum of the endo- and epicardial segment lengths from all three sections. Infarct size (in %) was calculated as the total infarct circumference divided by the total circumference times 100.

Measurement of blood pressure and heart rate during intracisternal administration of L-NMMA. In a separate group of animals, we examined the effects of intracisternal injection of N^G-monomethyl-L-arginine (L-NMMA), a NOS inhibitor, on blood pressure in the MI and sham-operated mice (n = 6 mice each) to confirm that the NOS activity was altered in MI mice. Four weeks after LCA ligation, the mice were anesthetized with pentobarbital sodium (50 mg/kg ip) and mechanically ventilated with room air supplemented with oxygen. A catheter was introduced into the left femoral vein for the administration of anesthetics. Another catheter was introduced into the aorta through the femoral artery to monitor and record systemic arterial pressure. The mice were placed in a stereotaxic frame, the dorsal surface of the medulla was then exposed, and the tip of a polyethylene tube (PE-10) was placed into the cisterna magna. Bolus injections of L-NMMA (100 nmol, 10 μl) were made through this tube. The drugs were dissolved in artificial cerebrospinal fluid containing (in mM) 123 NaCl, 0.86 $CaCl_2$, 3.0 KCl, 0.89 $MgCl_2$, 25 $NaHCO_3$, 0.5 NaH_2PO_4, and 0.25 Na_2HPO_4; pH 7.4.

Construction and purification of recombinant adenovirus. We used adenoviral vectors encoding either the bacterial β-galactosidase (Adβgal) gene or bovine endothelial NOS (eNOS) gene (6, 30). A replication-deficient adenovirus encoding the bovine eNOS gene expressed from a long-terminal repeat of the *Rous sarcoma* virus as a promoter was generated by using standard methods from the University of Iowa Gene Transfer Vector Core (Iowa City, IA) (6, 30). These vectors were suspended in PBS with 3% sucrose and stored at −80°C until use.

In vivo gene transfer into NTS. Four weeks after LCA ligation, mice were anesthetized with pentobarbital sodium (25–40 mg/kg ip), placed on a stereotaxic frame, and the dorsal surface of the medulla was exposed. A glass micropipette (5 μm, outer diameter) was filled with PBS containing Adβgal or AdeNOS. Bilateral injections were made into the NTS. One microinjection site in each NTS was defined according to a mouse atlas (35). An adenoviral suspension containing 1×10^8 plaque forming units per milliliter was injected into each injection site over 10 min (200 nl/each NTS; infusion rate, ~40 nl/min). After the injection, all mice recovered from the anesthesia and were unrestrained and free to move in their cages.

Histochemical analysis of β-galactosidase gene expression. On *day 7* after the gene transfer, the mice were deeply anesthetized with pentobarbital sodium (100 mg/kg ip) and perfused transcardially with PBS, followed by 4% paraformaldehyde in PBS. The brains were removed, and the coronal sections of the medulla were cut serially (50 μm) using a vibratome. The sections of the medulla were evaluated for β-galactosidase expression by histostaining with X-Gal in PBS at 37°C for 4 h.

Quantification of β-galactosidase activity. We quantified β-galactosidase activity in the mice (n = 4 mice at each time point) transfected with Adβgal with a colorimetric assay using *o*-nitrophenyl-β-D-galactopyranosidase (Boehringer Mannhein Biochemica; Mannheim, Germany) as described previously (2, 9, 17), before and on *days 1, 3, 5, 7, 10, 14, 21,* and *28* after the transfection of Adβgal.

Immunohistochemistry for eNOS and nNOS. In another group of animals, sheep anti-nNOS antibody (kindly provided by P. Emson, Department of Neurobiology, The Babraham Institute, Cambridge, UK) was used for an immunohistochemical analysis of endogenous nNOS (19). Four weeks after LCA ligation, serial sections of the medulla were obtained. The sections were incubated in sheep anti-nNOS antibody (1:10,000) and then rinsed in PBS. After overnight incubation in biotinylated donkey anti-sheep IgG (1:1,000, Jackson; Baltimore, MD), the sections were rinsed in PBS and incubated in a mixture of streptavidin-conjugated fluorescein isothiocyanate (1:200; Vector; Burlingame, CA). After being rinsed in PBS, the sections were mounted in Vectashield (Vector). In a separate group of mice transfected with AdeNOS, we performed immunohistochemistry for eNOS as described previously (22, 39). On *day 7* after the gene transfer, the sections were incubated in rabbit anti-eNOS IgG (1:200; Transduction; Lexington, KY) at room temperature overnight and then rinsed three times in PBS. After incubation with biotinylated horse anti-rabbit IgG (1:1,000, Vector), the sections were rinsed in PBS and incubated in a mixture of streptavidin-conjugated rhodamine (1:100, Vector). After being rinsed in PBS, the sections were mounted in Vectashield (Vector). The stained sections were photographed by using a confocal laser scanning microscope (MRC 1000, Bio-Rad; mounted on a Nikon light microscope Optiphot, Hemel Hempstead, UK) using laser beams of 488 nm for nNOS-stained sections and 580 nm for eNOS-stained sections for excitation with appropriate filter sets. Confocal images were then transferred to a personal computer and analyzed by using the National Institutes of Health Image program.

Western blot analysis for eNOS and nNOS. We performed Western blot analysis to determine the level of endogenous nNOS protein expression in MI mice. We also performed Western blot analysis to determine the time course of eNOS protein expression in AdeNOS-transfected mice. A coronal block of the brain (n = 4 mice for each line) containing the NTS was dissected, and the NTS tissues were obtained by using the punch microdissection technique (32, 33, 41) in MI mice and AdeNOS-transfected mice at 4 wk after LCA ligation and on *days 0, 3, 5, 7, 10, 14,* and *28* after AdeNOS transfer, respectively. The NTS tissues were homogenized and sonicated in a lysis buffer containing 40 mmol/l HEPES, 1% Triton X-100, 10% glycerol, and 1 mmol/l phenylmethylsulfonyl fluoride. The tissue lysate was centrifuged at 6,000 rpm for 5 min at 4°C using a microcentrifuge. The supernatant was collected, and the protein concentration was determined by using a bicinchoninic acid protein assay kit (Pierce Chemical; Rockford, IL). An aliquot of 5 μg of protein from each sample was separated on a sodium dodecyl sulfate gel and transferred electrophoretically onto polyvinylidene difluoride membranes (Immobilon-P membrane; Millipore, Bedford, MA). After we confirmed that equal amounts of protein were applied into each well using Ponceau S (Sigma Chemical, St. Louis, MO) staining, the membranes were incubated with either sheep anti-nNOS antibody (1:10,000) in MI mouse samples or rabbit anti-eNOS (1:200) in AdeNOS-transfected mouse samples. Membranes were then washed and incubated with a horseradish peroxidase conjugated horse anti-sheep IgG antibody (1:10,000) or horse anti-rabbit IgG (1:100,000), respectively. Immunoreactivity was detected by enhanced chemiluminescence autoradiography (ECL Western blotting detection kit; Amersham; Arlington Heights, IL).

Echocardiographic imaging. Four weeks after LCA ligation, i.e., just before the adenoviral gene transfer, serial two-dimensional and M-mode echocardiography was performed in all groups of animals under light pentobarbital sodium anesthesia with spontaneous respiration (15). An echocardiography system (SSD5000; Aloka, Tokyo) was used with a dynamically focused 10-MHz linear array transducer using a depth setting of 200 mm, as described previously (15, 28). Two-dimensional images and M-mode tracings were recorded from the short-axis view at the level of the papillary muscle. Care was taken to avoid applying too much pressure to the chest wall. The M-mode tracings were printed on glossy paper using a digital color printer (SSZ337). LV end-diastolic diameter (LVEDD), LV end-systolic diameter (LVESD), and wall thickness were measured, and the mean of three-to-five cardiac cycles was used for analysis. Percent fractional shortening (%FS) was calculated as follows: %FS = (LVEDD) − (LVESD)/(LVEDD) × 100. The same echocardiographic experiments were performed 6 and 8 wk after LCA ligation, i.e., 2 and 4 wk after AdeNOS gene transfer, respectively.

Measurement of urinary norepinephrine excretion. The urinary norepinephrine concentration was measured 4 wk after LCA ligation, i.e., just before gene transfer, and 7 days after the gene transfer by high-performance liquid chromatography, and urinary norepinephrine excretion over 24 h (μg/day) was then calculated as described previously (17, 22, 39).

Statistical analysis. All values were expressed as means ± SE. One-way ANOVA was used to compare the β-galactosidase activity. An unpaired *t*-test was used to compare values between the MI mice and sham-operated mice. Two-way ANOVA with repeated measures was used to compare the time course values of LVEDD and %FS between Adβgal and AdeNOS-transfected MI mice groups. A paired *t*-test was used to compare the values before and after each operation, or before and after the gene transfer, in sham-operated and MI mice. Differences were considered to be significant when $P < 0.05$.

RESULTS

HF characteristics of MI mice. Echocardiographic assessment of cardiac function was performed, and infarct size was estimated using Masson trichrome staining before and 4 wk after LCA ligation. Echocardiographic evaluation revealed that LVEDD was greater (5.2 ± 0.4 vs. 3.6 ± 0.2 mm; $P < 0.01$) and fractional shortening was smaller (19.1 ± 0.2% vs. 42.7 ± 0.1%; $P < 0.01$) in MI mice than in sham-operated mice (n = 11, each group) (Fig. 1, *A* and *B*). Examples of coronal sections of the LV are shown in Fig. 1, *C* and *D*. Infarct size of MI mice was 42.5 ± 2.3% (see Fig. 1, *C* and *D*). Furthermore, 24-h urinary norepinephrine excretion was significantly higher in MI mice compared with that in sham-operated mice (MI mice, 0.33 ± 0.06 μg; sham mice, 0.18 ± 0.03 μg; n = 13 mice for each group, $P < 0.05$). There was no difference in 24-h urinary volume between MI mice and sham-operated mice (data not shown).

Brain stem nNOS is reduced in HF. In this model, we evaluated nNOS protein expression in the brain stem by Western blot analysis and immunohistochemistry 4 wk after LCA ligation. Western blot analysis for nNOS in the NTS revealed reduced nNOS protein levels in MI mice compared with sham-operated mice (Fig. 2*A*). Immunohistochemical staining for nNOS protein was reduced in MI mice compared with that in sham-operated mice (Fig. 2, *B* and *C*).

Effect of intracisternal injection of L-NMMA on blood pressure. To determine whether endogenous NOS activity was altered in MI mice, we examined the effects of intracisternal injection of L-NMMA on blood pressure in sham-operated and

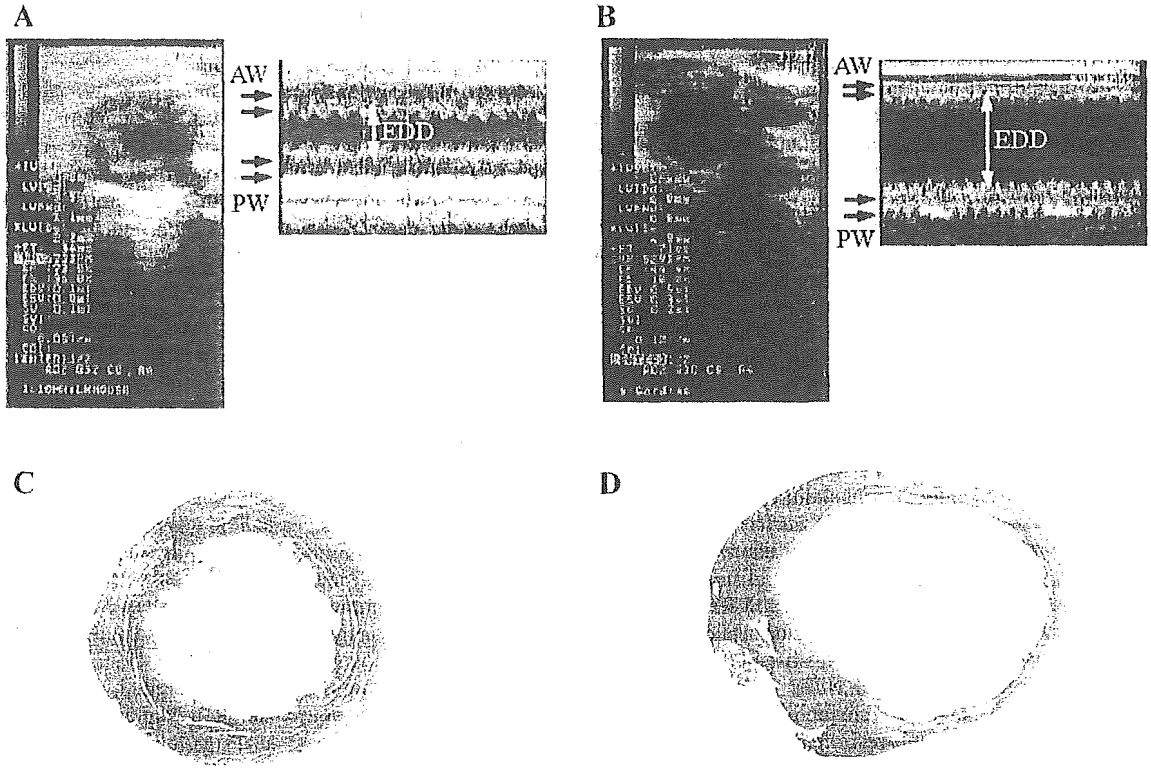

Fig. 1. B-mode and M-mode echocardiograms of left ventricular (LV) in parasternal short-axis view obtained from sham-operated (*A*) and myocardial infarction (MI) (*B*) mice. EDD, end-diastolic diameter; AW, anterior wall; PW posterior wall. MI mice exhibited LV dilatation and decreased fractional shortening. Low-power photograph of Masson-trichrome-stained LV cross-section was obtained from sham-operated (*C*) and MI (*D*) mice.

MI mice. Intracisternal injection of L-NMMA elicited a smaller increase in blood pressure in MI mice than in sham-operated mice (6.9 ± 3.4 vs. 20.6 ± 4.9 mmHg; $P < 0.05$) (Fig. 3*B*).

Effect of eNOS overexpression in NTS. Figure 4*A* shows the X-Gal staining for β-galactosidase in a section of the mouse brain medulla on *day 7* after the gene transfer. Positive staining for β-galactosidase was observed in the NTS where Adβgal had been microinjected. In the AdeNOS-transfected mice, eNOS protein expression was observed immunohistochemically in the NTS where AdeNOS had been microinjected (Fig. 4*B*). Figure 4*C* shows the time course of β-galactosidase activity before and after Adβgal transfection. The β-galactosidase activity in the medulla peaked on *day 7* and then declined over time. Figure 4*D* shows the time course of eNOS protein expression as determined by Western blot analysis. eNOS protein expression peaked at *day 7* and then declined over time until *day 28*. Urinary norepinephrine excretion in MI mice transfected with Adβgal or AdeNOS was also measured. Urinary norepinephrine excretion did not differ before adenoviral gene transfer (Fig. 5). Urinary norepinephrine excretion after transfection with AdeNOS, however, was significantly lower than before transfection with AdeNOS. In addition, after the gene transfer, urinary norepinephrine excretion in AdeNOS-transfected MI mice was significantly lower than in Adβgal-transfected MI mice. There was no change in 24-h urinary volume after AdeNOS transfection (data not shown). Adenoviral-mediated eNOS gene delivery did not improve the LV systolic function determined by EDD and %FS (Table 1).

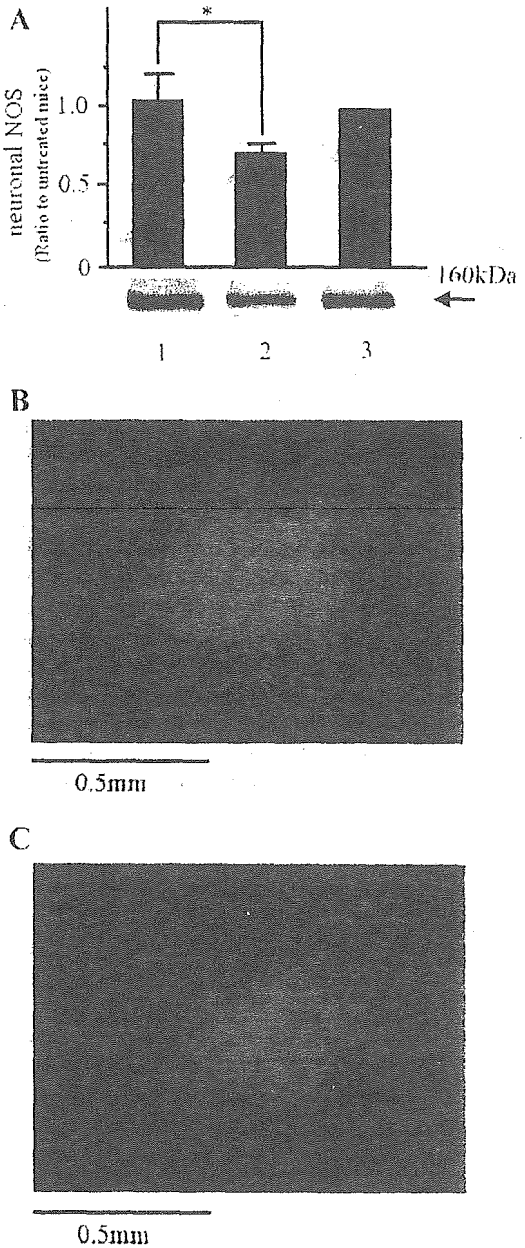

Fig. 2. Western blot analysis in nucleus tractus solitarius (NTS) demonstrating reduction in endogenous neuronal nitric oxide synthase (nNOS) protein in MI mice ($n = 4$ mice for each) *A*: *lane 1*, sham-operated mouse; *lane 2*, MI mouse; *lane 3*, untreated mouse. Immunohistochemical staining visualized with rhodamine-conjugated fluoroprobe for endogenous nNOS protein within NTS tissue in sham-operated (*B*) and MI (*C*) mice. *$P < 0.05$ compared with the value of sham-operated mice.

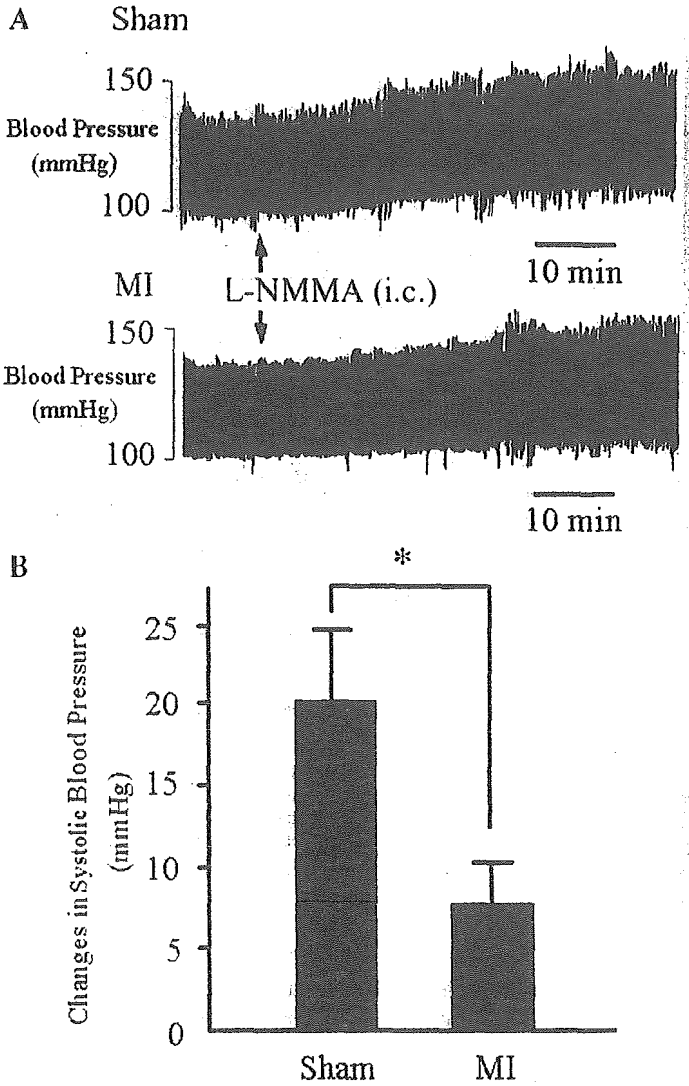

Fig. 3. Typical effects (*A*) and summary (*B*) observed in blood pressure changes after intracisternal (i.c.) injection of N^G-monomethyl-L-arginine (L-NMMA) in sham-operated and MI (*B*) mice, suggesting that NOS activity was reduced in MI mice ($n = 6$ mice for each, *$P < 0.05$).

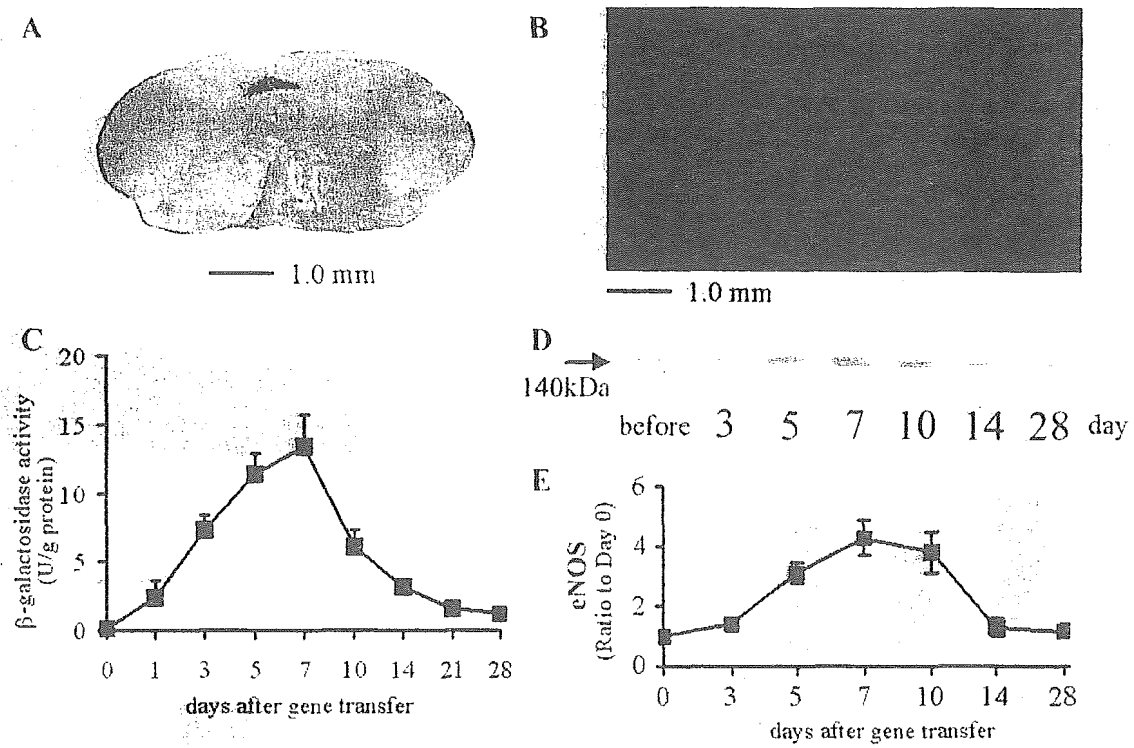

Fig. 4. Site-specific expression of β-galactosidase or endothelial NOS (eNOS) protein within NTS. *A*: dark blue X-Gal staining was observed locally in NTS of Adβgal-transfected mice. *B*: images of section of medulla stained with anti-eNOS antibody (red, visualized with rhodamine-conjugated fluoroprobe). *C*: eNOS-immunopositive sites are also detected locally in bilateral NTS of AdeNOS-injected mice. Time course of β-galactosidase activity in medulla transfected with Adβgal. β-Galactosidase activity was quantified by using colorimetric assay (n = 4 mice at each time point). *D* and *E*: time course of eNOS protein expression in medulla transfected with AdeNOS by Western blot analysis.

DISCUSSION

The major findings of the present study are as follows. First, the characteristics of MI mice were consistent with those of HF, a particularly increased activation of the sympathetic nervous system as determined by an increase in urinary norepinephrine excretion. Second, nNOS expression levels were significantly reduced in this MI mouse model. Finally, increased NO production induced by eNOS overexpression in the NTS in MI mice reduced urinary norepinephrine excretion to the levels of the sham-operated mice, suggesting that increased NO production in the NTS reduced the enhanced sympathetic drive in MI mice. Taken together, these results indicate that decreased NO in the brain, especially in the NTS, contributes to the enhanced sympathetic drive observed in HF.

MI mouse model of HF. HF was produced by coronary artery ligation in mice. This model is often used as a model of LV remodeling, myocardial ischemia, and reperfusion injury (15, 24, 28, 36, 39, 40, 43). Little is known, however, regarding the neurohumoral aspects of this model in mice. In our study, we demonstrated that urinary norepinephrine excretion measured

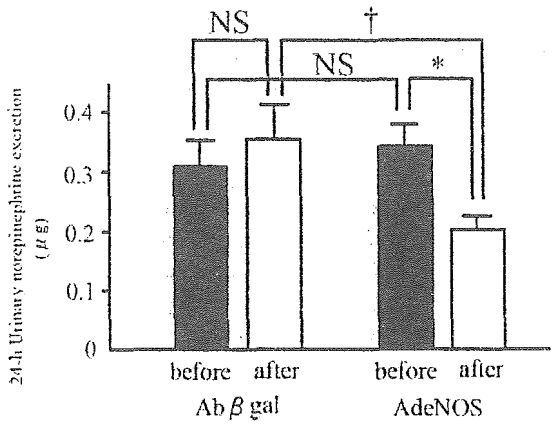

Fig. 5. Twenty-four-hour urinary norepinephrine excretion (in μg) before and after gene transfer in AdeNOS- and Adβgal-transfected MI mice. NS, not significant. *$P < 0.05$; †$P < 0.01$.

Table 1. *Time course of LV end-diastolic diameter and %FS in MI and sham-operated mice transfected with either Adβgal or AdeNOS*

	Sham Mice		MI Mice	
	AdeNOS	Adβgal	AdeNOS	Adβgal
n	10	7	9	6
	LV end-diastolic diameter, mm			
Before LCA Ligation	3.7±0.2	3.6±0.2	5.3±0.3	5.2±0.4
2 Wk	3.6±0.3	3.7±0.3	5.3±0.4	5.4±0.6
4 Wk	3.8±0.3	3.8±0.3	4.9±0.5	5.2±0.9
	%FS			
Before LCA Ligation	45.5±0.2	42.7±0.3	19.7±0.9	19.1±0.9
4 Wk	44.2±0.3	44.9±0.3	22.7±1.2	20.8±1.7
8 Wk	39.1±0.4	40.5±0.3	24.7±1.4	19.3±1.5

Values are means ± SE; n, number of mice. LV, left ventricular; % FS, percent fractional shortening; MI, myocardial infarction; Adβgal and AdeNOS, adenoviral vectors encoding β-galactosidase or endothelial nitric oxide synthase, respectively.

in a conscious state, which is a marker of sympathetic nerve activity, was significantly increased in mice 4 wk after MI. Consistent with the results of previous studies from Takeshita's laboratory (15), LV dilatation and reduced LV systolic function were also observed.

Sympathoexcitation in HF and role of NO in brain stems. HF is characterized by an enhanced neurohumoral drive in experimental animals as well as in patients (27, 29, 55). In patients with HF, plasma norepinephrine levels increase with severity and relate to the mortality rate (4, 38). The mechanism(s) underlying the sympathoexcitation observed in HF is not fully understood. Although it has been thought that abnormal arterial baroreflex and cardiopulmonary baroreflex control of sympathetic nerve activity are responsible for the sympathoexcitation in HF, recent studies (27, 29, 55) suggest that involvement of the CNS is important. Many studies (10, 27, 29, 55) predict an important role of angiotensin II, particularly in the forebrain, in HF. Liu and Zucker (25) suggested that a loss of NO and an increase in angiotensin II are necessary for sustained increases in sympathetic nerve activity in HF. In fact, inhibition of angiotensin II type I receptors in the NTS reduces arterial blood pressure, heart rate, and sympathetic nerve activity in rats with chronic inhibition of NOS (8). Previous studies from our laboratories and others (17, 22, 39) have established that NO in the brain inhibits sympathetic nerve activity. There are few studies (34, 54), however, regarding NO in the brain, especially the NTS, in HF. Patel et al. (33) reported decreased nNOS gene mRNA expression levels in the hypothalamus, dorsal pons, and dorsal medulla of rats with MI compared with those in sham-operated rats. In addition, the number of NADPH-diaphorase-positive neurons, a marker of nNOS activity, was significantly decreased in the PVN (54). In animal models of HF, blunted NO inhibition mediated sympathoexcitation in the PVN (53) and reduced central NO-mediated enhanced sympathetic afferent baroreflex gain (26).

In the present study, nNOS expression evaluated by Western blot analysis and immunohistochemical staining in the brain stem, particularly in the NTS, was reduced in HF mice compared with that in sham-operated mice. Also, the pressor response evoked by intracisternal injection of L-NMMA was lower in MI mice compared with that in sham-operated mice, suggesting that NOS activity in the NTS is reduced in our MI mouse model.

Effect of eNOS overexpression in NTS. The most important finding of the present study is that the increase in urinary norepinephrine excretion in MI mice was significantly reduced compared with that in the sham-operated mice after eNOS overexpression in the NTS in a conscious state. This finding indicates that an increase in NO production in the NTS normalizes the enhanced sympathetic drive observed in HF. In the present study, we transfected adenoviral vectors encoding either the β-galactosidase gene or the eNOS gene into the NTS of mice in vivo, which was confirmed by Western blot analysis and immunohistochemical staining. Furthermore, consistent with previous studies from Takeshita's laboratory (39) using rats, the time course of β-galactosidase activity or eNOS expression peaked on *day 7* after the gene transfer. Because we (20) and others (44) previously demonstrated that overexpression of eNOS in the brain does not affect the nNOS expression levels, the maximum physiological effect of viral-mediated gene transfer was anticipated to occur on *day 7* after the gene transfer. Therefore, we measured urinary norepinephrine excretion on *day 7* after the gene transfer. As discussed in previous studies (17, 22, 39) using this technique, we used eNOS instead of nNOS, which normally exists in the CNS, because the purpose of this study was to increase the local NO production in the NTS for a relatively long period in mice transfected with AdeNOS. We previously demonstrated that this method is useful for examining the effect of NO overproduction in a specific nucleus of the brain on cardiovascular regulation in conscious animals (17, 22, 39). The increase in NOS expression in the NTS attenuated the increase in urinary norepinephrine excretion, which is a marker of sympathetic nerve activity, in MI mice in a conscious state. These results suggest that the reduced NO production in the NTS contributes to the enhanced sympathetic drive in HF.

Waki et al. (49) reported that chronic inhibition of endogenous eNOS in the caudal NTS enhances baroreflex and suggested that NO might be functionally diverse within the NTS. In the present study, we did not address the role of endogenous NO released from neurons and endothelium (34) on the baroreflex function in HF. There are functionally discrete subregions that exhibit a different response to the same neuropeptide, even within the NTS (45). Thus various results between the caudal subregion of the NTS in the study by Waki et al. (49) and the entire NTS in the present study might reflect the diverse physiological functions of NO based on discrete subgroups of neurons within the NTS.

A recent study (51) indicated that NO in a different brain stem nucleus, the rostral ventrolateral medulla, also improves HF pathophysiology. Therefore, increasing NO in the brain stem might be a new therapeutic target for the treatment of HF from the aspect of neurohumoral activation.

Study limitations. It is possible that the reduced blood pressure response to L-NMMA in mice with HF was due to elevated basal sympathetic nerve activity that cannot be further increased. This possibility is unlikely, however, because the sympathetic nerve response to blocking the airway in HF rats was higher than that elicited by L-NMMA (53). Recently, it was suggested that NADPH-dependent superoxide anions are increased in the brain in experimental chronic HF and that increased reactive oxygen species in the brain contribute to increased sympathetic nerve activity (12, 21, 24). Because brain NO might be trapped by increased superoxide anions in chronic HF states, it is possible that the sympathoexcitation in HF is determined by the balance between NO and reactive oxygen species. Further studies are required to elucidate this point.

We found that eNOS gene transfer in the NTS normalized the enhanced sympathetic drive observed in our HF model. We measured urinary norepinephrine excretion as a marker of sympathetic nerve activity. Direct measurement of sympathetic nerve activity is preferable, but it is technically difficult to perform in conscious mice. Because the expression of the gene using adenovirus vectors remains high enough for only several days, this technique does not allow us to observe an improvement in survival (data not shown) or inhibition of LV remodeling (Table 1). Further experiments to examine the long-term effect of an increase in NO within the brain stem in HF are important. Another efficient vector system that expresses the gene for a longer period, such as the adenovirus-associated virus (37) or feline immunodeficiency virus (42),

might be useful for examining the long-term effect of NO in the NTS on HF.

In conclusion, MI mice have characteristics consistent with HF, particularly from the aspect of sympathetic nervous system activation. This activation is mediated, at least in part, by decreases in nNOS expression, resulting in decreased NO production in the NTS. Overexpression of eNOS in the NTS decreases urinary norepinephrine excretion, suggesting that increased NO production in the brain stem, particularly in the NTS, reduces the enhanced sympathetic drive observed in HF.

ACKNOWLEDGMENTS

The authors thank Drs. D. D. Heistad and B. L. Davidson (The University of Iowa Gene Transfer Vector Core, supported by National Institutes of Health grants and the Carver Foundation) for the preparation of vectors. We thank Dr. P. Emson for kindly providing the sheep antibody to nNOS. We also thank Dr. T. Kosaka for advice in the immunohistochemical analysis for eNOS and the use of his facility for microscopic analysis.

GRANTS

This work was supported by a Grant-in-Aid for Scientific Research (C)11670689) from the Ministry of Education, Science, Sports, and Culture and the Japan Society for the Promotion of Science.

REFERENCES

1. **Andresen MC and Kunze DL.** Nucleus tractus solitarius–gateway to neural circulatory control. *Annu Rev Physiol* 56: 93–116, 1994.
2. **Bradford MM.** A rapid and sensitive method for the quantitation of microgram quantities of protein utilizing the principle of protein-dye binding. *Anal Biochem* 72: 248–254, 1976.
3. **Bristow MR, O'Connell JB, Gilbert EM, French WJ, Leatherman G, Kantrowitz NE, Orie J, Smucker ML, Marshall G, and Kelly P.** Dose-response of chronic beta-blocker treatment in heart failure from either idiopathic dilated or ischemic cardiomyopathy. Bucindolol Investigators. *Circulation* 89: 1632–1642, 1994.
4. **Cohn JN, Levine TB, Olivari MT, Garberg V, Lura D, Francis GS, Simon AB, and Rector T.** Plasma norepinephrine as a guide to prognosis in patients with chronic congestive heart failure. *N Engl J Med* 311: 819–823, 1984.
5. **Dampney RA.** Functional organization of central pathways regulating the cardiovascular system. *Physiol Rev* 74: 323–364, 1994.
6. **Davidson BL, Allen ED, Kozarsky KF, Wilson JM, and Roessler BJ.** A model system for in vivo gene transfer into the central nervous system using an adenoviral vector. *Nat Genet* 3: 219–223, 1993.
7. **De Vente J, Hopkins DA, Markerink-Van Ittersum M, Emson PC, Schmidt HH, and Steinbusch HW.** Distribution of nitric oxide synthase and nitric oxide-receptive, cyclic GMP-producing structures in the rat brain. *Neuroscience* 87: 207–241, 1998.
8. **Eshima K, Hirooka Y, Shigematsu H, Matsuo I, Koike G, Sakai K, and Takeshita A.** Angiotensin in the nucleus tractus solitarii contributes to neurogenic hypertension caused by chronic nitric oxide synthase inhibition. *Hypertension* 36: 259–263, 2000.
9. **Eustice DC, Feldman PA, Colberg-Poley AM, Buckery RM, and Neubauer RH.** A sensitive method for the detection of beta-galactosidase in transfected mammalian cells. *Biotechniques* 11: 739–740, 1991.
10. **Felder RB, Francis J, Weiss RM, Zhang ZH, Wei SG, and Johnson AK.** Neurohumoral regulation in ischemia-induced heart failure. Role of the forebrain. *Ann NY Acad Sci* 940: 444–453, 2001.
11. **Francis GS, Benedict C, Johnstone DE, Kirlin PC, Nicklas J, Liang CS, Kubo SH, Rudin-Toretsky E, and Yusuf S.** Comparison of neuroendocrine activation in patients with left ventricular dysfunction with and without congestive heart failure. A substudy of the Studies of Left Ventricular Dysfunction (SOLVD). *Circulation* 82: 1724–1729, 1990.
12. **Gao L, Wang W, Li YL, Schultz HD, Liu D, Cornish KG, and Zucker IH.** Superoxide mediates sympathoexcitation in heart failure: roles of angiotensin II and NAD(P)H oxidase. *Circ Res* 95: 937–944, 2004.
13. **Hara H, Waeber C, Huang PL, Fujii M, Fishman MC, and Moskowitz MA.** Brain distribution of nitric oxide synthase in neuronal or endothelial nitric oxide synthase mutant mice using [^{3}H]L-N^G-nitro-arginine autoradiography. *Neuroscience* 75: 881–890, 1996.
14. **Harada S, Tokunaga S, Momohara M, Masaki H, Tagawa T, Imaizumi T, and Takeshita A.** Inhibition of nitric oxide formation in the nucleus tractus solitarius increases renal sympathetic nerve activity in rabbits. *Circ Res* 72: 511–516, 1993.
15. **Hayashidani S, Tsutsui H, Shiomi T, Suematsu N, Kinugawa S, Ide T, Wen J, and Takeshita A.** Fluvastatin, a 3-hydroxy-3-methylglutaryl coenzyme a reductase inhibitor, attenuates left ventricular remodeling and failure after experimental myocardial infarction. *Circulation* 105: 868–873, 2002.
16. **Hironaga K, Hirooka Y, Matsuo I, Shihara M, Tagawa T, Harasawa Y, and Takeshita A.** Role of endogenous nitric oxide in the brain stem on the rapid adaptation of baroreflex. *Hypertension* 31: 27–31, 1998.
17. **Hirooka Y, Sakai K, Kishi T, and Takeshita A.** Adenovirus-mediated gene transfer into the NTS in conscious rats. A new approach to examining the central control of cardiovascular regulation. *Ann NY Acad Sci* 940: 197–205, 2001.
18. **Hirooka Y, Shigematsu H, Kishi T, Kimura Y, Ueta Y, and Takeshita A.** Reduced nitric oxide synthase in the brain stem contributes to enhanced sympathetic drive in rats with heart failure. *J Cardiovasc Pharmacol* 42, *Suppl* 1: S111–S115, 2003.
19. **Jinno S, Aika Y, Fukuda T, and Kosaka T.** Quantitative analysis of neuronal nitric oxide synthase-immunoreactive neurons in the mouse hippocampus with optical disector. *J Comp Neurol* 410: 398–412, 1999.
20. **Kishi T, Hirooka Y, Ito K, Sakai K, Shimokawa H, and Takeshita A.** Cardiovascular effects of overexpression of endothelial nitric oxide synthase in the rostral ventrolateral medulla in stroke-prone spontaneously hypertensive rats. *Hypertension* 39: 264–268, 2002.
21. **Kishi T, Hirooka Y, Kimura Y, Ito K, Shimokawa H, and Takeshita A.** Increased reactive oxygen species in rostral ventrolateral medulla contribute to neural mechanisms of hypertension in stroke-prone spontaneously hypertensive rats. *Circulation* 109: 2357–2362, 2004.
22. **Kishi T, Hirooka Y, Sakai K, Shigematsu H, Shimokawa H, and Takeshita A.** Overexpression of eNOS in the RVLM causes hypotension and bradycardia via GABA release. *Hypertension* 38: 896–901, 2001.
23. **Kumada M, Terui N, and Kuwaki T.** Arterial baroreceptor reflex: its central and peripheral neural mechanisms. *Prog Neurobiol* 35: 331–361, 1990.
24. **Lindley TE, Doobay MF, Sharma RV, and Davisson RL.** Superoxide is involved in the central nervous system activation and sympathoexcitation of myocardial infarction-induced heart failure. *Circ Res* 94: 402–409, 2004.
25. **Liu JL and Zucker IH.** Regulation of sympathetic nerve activity in heart failure: a role for nitric oxide and angiotensin II. *Circ Res* 84: 417–423, 1999.
26. **Ma R, Zucker IH, and Wang W.** Reduced NO enhances the central gain of cardiac sympathetic afferent reflex in dogs with heart failure. *Am J Physiol Heart Circ Physiol* 276: H19–H26, 1999.
27. **Mark AL.** Sympathetic dysregulation in heart failure: mechanisms and therapy. *Clin Cardiol* 18: I3–I8, 1995.
28. **Michael LH, Entman ML, Hartley CJ, Youker KA, Zhu J, Hall SR, Hawkins HK, Berens K, and Ballantyne CM.** Myocardial ischemia and reperfusion: a murine model. *Am J Physiol Heart Circ Physiol* 269: H2147–H2154, 1995.
29. **Middlekauff HR and Mark AL.** The treatment of heart failure: the role of neurohumoral activation. *Intern Med* 37: 112–122, 1998.
30. **Ooboshi H, Chu Y, Rios CD, Faraci FM, Davidson BL, and Heistad DD.** Altered vascular function after adenovirus-mediated overexpression of endothelial nitric oxide synthase. *Am J Physiol Heart Circ Physiol* 273: H265–H270, 1997.
31. **Packer M, Bristow MR, Cohn JN, Colucci WS, Fowler MB, Gilbert EM, and Shusterman NH.** The effect of carvedilol on morbidity and mortality in patients with chronic heart failure. U.S. Carvedilol Heart Failure Study Group. *N Engl J Med* 334: 1349–1355, 1996.
32. **Palkovits M.** Punch sampling biopsy technique. *Methods Enzymol* 103: 368–376, 1983.
33. **Patel KP, Zhang K, Zucker IH, and Krukoff TL.** Decreased gene expression of neuronal nitric oxide synthase in hypothalamus and brain stem of rats in heart failure. *Brain Res* 734: 109–115, 1996.
34. **Paton JF, Deuchars J, Ahmad Z, Wong LF, Murphy D, and Kasparov S.** Adenoviral vector demonstrates that angiotensin II-induced depression of the cardiac baroreflex is mediated by endothelial nitric oxide synthase in the nucleus tractus solitarii of the rat. *J Physiol* 531: 445–458, 2001.

35. **Patrick RH, Warren GY, Floyd EB, Pavel VB, and Marco RC.** *Comparative Cytoarchitectonic Atlas of the C57BL//6 and 129/Sv Mouse Brains.* Amsterdam: Elsevier Science, 2000.
36. **Patten RD, Aronovitz MJ, Deras-Mejia L, Pandian NG, Hanak GG, Smith JJ, Mendelsohn ME, and Konstam MA.** Ventricular remodeling in a mouse model of myocardial infarction. *Am J Physiol Heart Circ Physiol* 274: H1812–H1820, 1998.
37. **Phillips MI.** Antisense inhibition and adeno-associated viral vector delivery for reducing hypertension. *Hypertension* 29: 177–187, 1997.
38. **Rector TS, Olivari MT, Levine TB, Francis GS, and Cohn JN.** Predicting survival for an individual with congestive heart failure using the plasma norepinephrine concentration. *Am Heart J* 114: 148–152, 1987.
39. **Sakai K, Hirooka Y, Matsuo I, Eshima K, Shigematsu H, Shimokawa H, and Takeshita A.** Overexpression of eNOS in NTS causes hypotension and bradycardia in vivo. *Hypertension* 36: 1023–1028, 2000.
40. **Scherrer-Crosbie M, Steudel W, Ullrich R, Hunziker PR, Liel-Cohen N, Newell J, Zaroff J, Zapol WM, and Picard MH.** Echocardiographic determination of risk area size in a murine model of myocardial ischemia. *Am J Physiol Heart Circ Physiol* 277: H986–H992, 1999.
41. **Shigematsu H, Hirooka Y, Eshima K, Shihara M, Tagawa T, and Takeshita A.** Endogenous angiotensin II in the NTS contributes to sympathetic activation in rats with aortocaval shunt. *Am J Physiol Regul Integr Comp Physiol* 280: R1665–R1673, 2001.
42. **Sinnayah P, Lindley TE, Staber PD, Cassell MD, Davidson BL, and Davisson RL.** Selective gene transfer to key cardiovascular regions of the brain: comparison of two viral vector systems. *Hypertension* 39: 603–608, 2002.
43. **Suzuki M, Sasaki N, Miki T, Sakamoto N, Ohmoto-Sekine Y, Tamagawa M, Seino S, Marban E, and Nakaya H.** Role of sarcolemmal K(ATP) channels in cardioprotection against ischemia/reperfusion injury in mice. *J Clin Invest* 109: 509–516, 2002.
44. **Tai MH, Wang LL, Wu KL, and Chan JY.** Increased superoxide anion in rostral ventrolateral medulla contributes to hypertension in spontaneously hypertensive rats via interactions with nitric oxide. *Free Radic Biol Med* 38: 450–462, 2005.
45. **Tan PS, Potas JR, Killinger S, Horiuchi J, Goodchild AK, Pilowsky PM, and Dampney RA.** Angiotensin II evokes hypotension and renal sympathoinhibition from a highly restricted region in the nucleus tractus solitarii. *Brain Res* 1036: 70–76, 2005.
46. **Tseng CJ, Liu HY, Lin HC, Ger LP, Tung CS, and Yen MH.** Cardiovascular effects of nitric oxide in the brain stem nuclei of rats. *Hypertension* 27: 36–42, 1996.
47. **Vincent SR and Kimura H.** Histochemical mapping of nitric oxide synthase in the rat brain. *Neuroscience* 46: 755–784, 1992.
48. **Waagstein F, Bristow MR, Swedberg K, Camerini F, Fowler MB, Silver MA, Gilbert EM, Johnson MR, Goss FG, and Hjalmarson A.** Beneficial effects of metoprolol in idiopathic dilated cardiomyopathy. Metoprolol in Dilated Cardiomyopathy (MDC) Trial Study Group. *Lancet* 342: 1441–1446, 1993.
49. **Waki H, Kasparov S, Wong LF, Murphy D, Shimizu T, and Paton JF.** Chronic inhibition of endothelial nitric oxide synthase activity in nucleus tractus solitarii enhances baroreceptor reflex in conscious rats. *J Physiol* 546: 233–242, 2003.
50. **Wang Y, Liu XF, Cornish KG, Zucker IH, and Patel KP.** Effects of nNOS antisense in the paraventricular nucleus on blood pressure and heart rate in rats with heart failure. *Am J Physiol Heart Circ Physiol* 288: H205–H213, 2005.
51. **Wang Y, Patel KP, Cornish KG, Channon KM, and Zucker IH.** nNOS gene transfer to RVLM improves baroreflex function in rats with chronic heart failure. *Am J Physiol Heart Circ Physiol* 285: H1660–H1667, 2003.
52. **Zanzinger J, Czachurski J, and Seller H.** Inhibition of sympathetic vasoconstriction is a major principle of vasodilation by nitric oxide in vivo. *Circ Res* 75: 1073–1077, 1994.
53. **Zhang K, Li YF, and Patel KP.** Blunted nitric oxide-mediated inhibition of renal nerve discharge within PVN of rats with heart failure. *Am J Physiol Heart Circ Physiol* 281: H995–H1004, 2001.
54. **Zhang K, Zucker IH, and Patel KP.** Altered number of diaphorase (NOS) positive neurons in the hypothalamus of rats with heart failure. *Brain Res* 786: 219–225, 1998.
55. **Zucker IH, Wang W, Brandle M, Schultz HD, and Patel KP.** Neural regulation of sympathetic nerve activity in heart failure. *Prog Cardiovasc Dis* 37: 397–414, 1995.

社団法人 電子情報通信学会
THE INSTITUTE OF ELECTRONICS,
INFORMATION AND COMMUNICATION ENGINEERS

信学技報
TECHNICAL REPORT OF IEICE.

生体の温度上昇評価による体内無線通信方式の検討

久世 直樹† 石橋 功至† 松田 慧† 原田 浩樹† 河野 隆二†

† 横浜国立大学大学院 工学府 物理情報工学専攻
〒 240-8501 神奈川県横浜市保土ヶ谷区常盤台 79 － 5
E-mail: †{kuse,ishibashi,matsuda,hhiroki,kohno}@kohnolab.dnj.ynu.ac.jp

あらまし 近年，生体内に医療機器を埋め込み，常時生体情報を得る無線通信に関する研究が行われている．自由空間における無線通信とは異なり，生体内においては健康への影響，特に熱影響を考慮した通信方式を検討する必要がある．本稿では送信機から放射された電磁波によって健康への影響が及ばないとされる上昇温度以下で通信を評価するためのモデルを提案する．これに基づき，低消費電力が期待される超広帯域無線通信の通信方式の評価を行い，OOK 変調の有用性を示す．

キーワード 生体内通信，SAR，超広帯域無線通信，OOK 変調，生体熱輸送方程式

A Study on In Vivo Wireless Communication Based on Body Temperature Elevation.

Naoki KUSE†, Koji ISHIBASHI†, Satoshi MATSUDA†, Hiroki HARADA†, and Ryuji KOHNO†

† Division of Electrical and Computer Engineering, Faculty of Engineering, Yokohama National University
79-5 Tokiwadai, Hodogaya-ku, Yokohama, 240-8501 Japan
E-mail: †{kuse,ishibashi,matsuda,hhiroki,kohno}@kohnolab.dnj.ynu.ac.jp

Abstract Recently, in vivo wireless communication technology in order to observe real-time biological information has been studied. Unlike free space propagation, in vivo wireless communication systems must consider health effects, especially thermal effects. Thus, in this paper, we propose an analysis model to evaluate thermal effects of radiated electromagnetic waves from a transmitter. Moreover, we also investigate ultra wideband (UWB) communication systems based on proposed model and show significant advantages of on-off keying (OOK) in terms of both health effects and system throughput.

Key words In-Vivo Communivation, SAR, UWB, OOK, Bio Heat Temperature Equation

1. はじめに

近年，体内にセンサを埋め込み，常時生体情報を得る医療情報通信技術に注目が集まっている．生体内に埋め込むセンサは長期間の運用も考えられることから，消費電力の抑制を考慮することが必須である．また，カプセル型内視鏡に代表されるような，生体内で撮影した大量の画像データを無線通信によって体外に伝送するシステムが考えられており，高速通信に対する要求も高まっている．このような要求が高まる一方，生体内での無線通信による発熱効果の人体への悪影響に対する懸念もある．これまで，携帯電話をはじめ，PHS，基地局などからの電磁波の暴露を想定した健康影響への評価が多くなされてきた．しかし，先に挙げた生体内無線通信の要求と安全性を共に考慮して評価した通信方式の検討は少ない．本稿では，送受信アンテナに微小ダイポールアンテナを用いて，熱影響を考慮したモデルを提案し，提案モデルに対してスループットの評価を行い，生体内に適した通信方式の検討を行った．従来の搬送波を用いた通信においては，眼球，睾丸，臓器等との共振現象により部分的に加温されてホットスポットが生じることも報告されてきた．そこで本稿の検討では，搬送波を用いる通信ではなく，より消費電力の低減，熱影響による低侵襲が期待できるUWB(Ultra Wideband) に関して検討を行う．

2. 生体への熱影響とモデル

2.1 電磁波による熱影響

電磁波による熱影響は SAR (Specific Absorption Rate) を用いて表される．これは携帯電話や無線基地局の生体への熱影響を評価する値として広く用いられ，SAR は式 (1) によって求

められる [1].

$$SAR = \frac{\sigma}{\rho} E^2 [W/kg] \quad (1)$$

σ は導電率，ρ は生体組織の密度，E は電界強度である．SAR は生物学的実験から，生体が 1 ℃以上の温度上昇を伴う電磁波により健康被害がでると報告されている [2]．これに基づき，1 ℃以上の温度上昇に相当する SAR が算出され，管理環境(注1)では安全率を 10 倍，一般環境(注2)では 50 倍の安全率をかけることで表 1 に示す電波防護指針が制定されている [3].

表 1　SAR 規制値

	管理環境	一般環境
全身平均 SAR (注3) $[W/kg]$	0.4	0.08
局所 SAR(注4) $[W/kg]$	10,20（四肢）	2,4（四肢）

これらは電磁波による暴露を想定した値となっている．暴露による温度上昇では，体表と外気による熱交換作用によって，冷却効果が加味される．しかし，今回問題とするのは，少なくとも送信が生体内に完全に埋め込まれた状況であるため，外気との熱交換作用は見込めない．これによって，放射された電磁波のほとんどは生体で吸収され，かつ上昇熱がこもることが予想される．以上の理由から，本指針をそのまま生体内通信の安全基準に適用する事はできない．そこで本稿では，生体に異常をきたす 1 ℃の温度上昇に対して，安全率 50 倍を想定し，0.02 ℃の温度上昇を許可しないモデルを次節で提案する．

2.2　モ　デ　ル

熱影響を伝送速度へのペナルティとして評価に加えるために下記のモデルを提案する．2.1 で挙げた安全基準を遵守するものとし，$T_{max} = 0.02$[℃] に加温された場合は $T_w = 0.01$[℃] 冷却されるまで通信を許可しない．フローチャートを図 1 に示す．

(1)　送受信は一対一とする．
(2)　雑音は加法性白色ガウス雑音（AWGN）とする．
(3)　損失媒質は均一で，境界を考えない．
(4)　受信アンテナは遠方界にあるとする．
(5)　許容上昇温度 T_{max} までの温度上昇を許可し，それ以上になる場合は無通信状態とする．
(6)　冷却効果により，T_{max} から T_w だけ低下した場合，通信を許可する．
(7)　温度の評価点は，送信アンテナの周囲 10g に当たる範囲を平均化して評価する d

モデル (6)(7) からデューティサイクルを導出する．通信可能時間を t_{on}，無通信時間を t_{off} とすると，デューティーサイクルは式 (2) で表される．時間による温度上昇とその変化の様子

(注1)：人体が電磁界にさらされている状況が認識され，電波の放射源を特定できるとともに，これに応じた適切な管理が行える環境条件
(注2)：人体が電磁界にさらされている状況の認識や適切管理等が期待できず，不確定な要因がある環境
(注3)：SAR を全身にわたり平均したもの
(注4)：SAR を人体局所の任意の組織 1g または 10g にわたり平均したもの

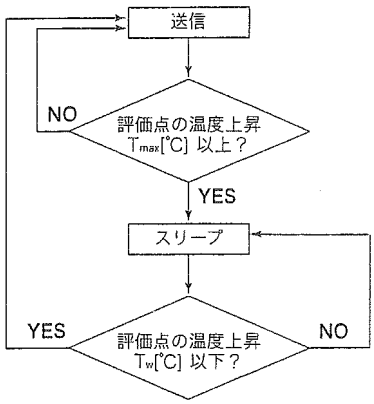

図 1　モデルのフローチャート

を図 2 に示す．モデルで示したように，上昇温度が 0.02[℃] に達した場合，スリープ状態となる．スリープ状態の場合は血液の冷却のみの効果によって体温は下降し，0.01[℃] まで冷却されると通信を再開する．

$$D_c = \frac{t_{on}}{t_{on} + t_{off}} \quad (2)$$

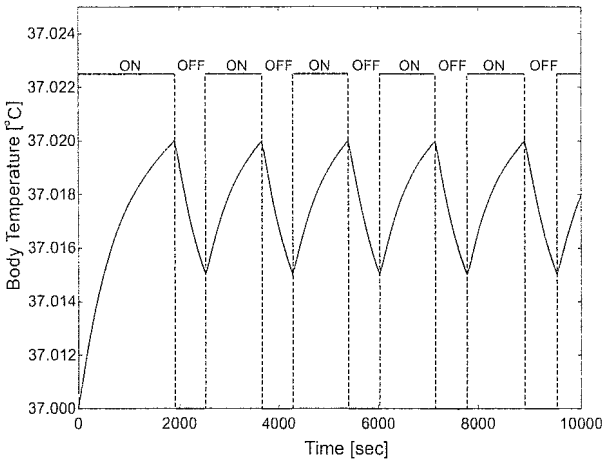

図 2　温度上昇とデューティーサイクル

2.3　生体内における熱伝搬

電磁波によって生じた熱の生体内における伝搬現象の計算手法として，生体熱輸送方程式を用いる [4]．これは，SAR の分布，生体定数から熱伝搬を計算する手法であり，さまざまな分野で用いられている．生体熱輸送方程式は (3) で表される．

$$\rho c \frac{\partial T}{\partial t} = \kappa \nabla^2 T - \rho \rho_b c_b F (T - T_b) + \rho SAR \quad (3)$$

c：生体組織の比熱 $[J/kg \cdot K]$，κ：生体組織の熱伝導率 $[W/m \cdot K]$，ρ：生体組織の密度 $[kg/m^3]$，ρ_b：血液の密度 $[kg/m^3]$，c_b：血液の比熱 $[J/kg \cdot K]$，T_b：血液の温度 [℃]，F：血液の流量率 $[m^3/kg \cdot s]$

上式 (3) の右辺第 1 項は周囲からの熱伝搬，第 2 項は血流による冷却効果であり，第 3 項は SAR による発熱効果を表す．ただし，以下の条件下において本式を導入する．

(1) 生体と外気による熱交換作用は安全側を議論するために考慮しない

(2) 計算領域の境界面においては 37.0 ℃一定とする

(3) 新陳代謝による発熱効果は他の熱効果に比べて小さいので考慮しない

(4) 動脈，静脈などの太い血管が通る組織ではなく，血流は毛細血管のみを考慮し均一とする

2.4 損失媒質中における微小ダイポールアンテナからの放射

損失媒質中での固有インピーダンス η は式 (4) であらわされる．

$$\eta = \frac{\gamma}{\sigma + j\omega\epsilon} \tag{4}$$

σ：導電率 $[S/m]$，ϵ：誘電率 $[F/m]$，ω：角周波数 $[rad/s]$

また，γ は伝搬定数であり，振幅減衰定数 α，位相変化定数 β を用いて，式 (5) で表される．

$$\gamma = \alpha + j\beta \tag{5}$$

ここで，減衰定数 $\alpha[Neper/m]$，位相定数 $\beta[rad/m]$ はそれぞれ式 (6),(7) から求められる．

$$\alpha = \omega\sqrt{\mu\epsilon}\sqrt{\frac{1}{2}(\sqrt{1+(\frac{\sigma}{\omega\epsilon})^2}-1)} \tag{6}$$

$$\beta = \omega\sqrt{\mu\epsilon}\sqrt{\frac{1}{2}(\sqrt{1+(\frac{\sigma}{\omega\epsilon})^2}+1)} \tag{7}$$

これらを用いて損失媒質内での微小ダイポールの任意点 (r,θ,ϕ) における放射電磁界は，入力電流スペクトル $P(\omega)$ を式 (8),(9),(10) に代入することで求めることができる [5]．

$$E_r(\omega) = \frac{2P(\omega)dl\cos\theta}{4\pi}e^{-jkr}(\frac{\eta}{r^2}+\frac{1}{j\omega\epsilon r^3}) \tag{8}$$

$$E_\theta(\omega) = \frac{P(\omega)dl\sin\theta}{4\pi}e^{-jkr}(\frac{j\omega\mu}{r}+\frac{\eta}{r^2}+\frac{1}{j\omega\epsilon r^3}) \tag{9}$$

$$H_\phi(\omega) = \frac{P(\omega)dl\sin\theta}{4\pi}e^{-jkr}(\frac{jk}{r}+\frac{1}{r^2}) \tag{10}$$

ただし，dl を微小ダイポールの長さとし，k は複素波数で，式 (11) から求められる．

$$k = -j\gamma = \beta - j\alpha \tag{11}$$

2.5 周波数領域における SAR

式 (1) より SAR を導出する際に，導電率は周波数に依存することを考慮しなければならない．図 3 には脂肪の導電率の周波数特性を示す．これからわかるように，広い帯域幅をもつ信号に対応する導電率を考えるとき，帯域幅の最大周波数と最小周波数成分ではその導電率に大きな差が生じるため，中心周波数での近似は誤差が大きくなる．そこで，孤立信号をフーリエ変換し，パーセバルの等式から周波数領域での積分値が時間領域での積分に対応することを利用する．SAR はその孤立波に反復率 R を乗じて得ることができる

$$SAR = \frac{R}{\rho}\int_{-\infty}^{\infty}\sigma(f)|E(f)|^2 df \tag{12}$$

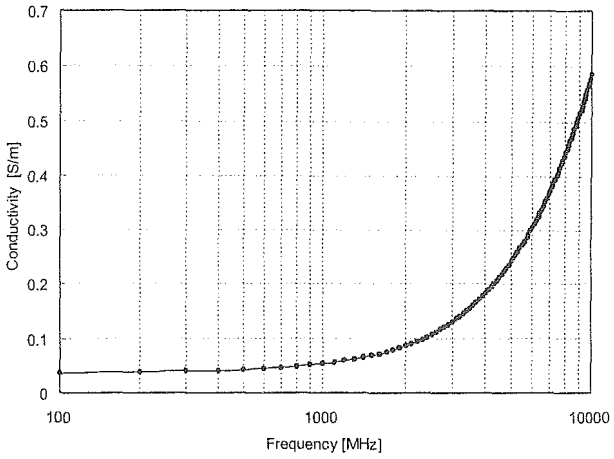

図 3 導電率の周波数特性

また，任意周波数における生体組織の電気特性は式 13 に示す Cole-Cole 近似式を用いて，複素誘電率から導出することができる．[6] [7]．

$$\dot{\varepsilon_r}(\omega) = \varepsilon_\infty + \sum_{n=1}^{4}\frac{\triangle\varepsilon_n}{1+(j\omega\tau_n)^{1-\alpha_n}} + \frac{\sigma_i}{j\omega\varepsilon_0} \tag{13}$$

ε_∞，ε_n，τ_n，α_n，σ_i は各組織に対応するパラメータである．

2.6 送受信電力

送信電力 P_T は，SAR の導出式 (1) より，電力と SAR の関係式から式 (14) のように表される．

$$\delta P = SAR \times \rho \times dV \tag{14}$$

これを全空間にわたり積分することで送信電力を得る

遠方界（距離 d）に受信アンテナをおいたとき，その受信電力は式 (15) で表される．

$$\begin{aligned} P_R &= P_e A_e \\ &= \frac{P_T - P_{Loss}}{4\pi d^2}G_t A_e \\ &= \frac{P_T - P_{Loss}}{(4\pi d)^2}G_t G_r \end{aligned} \tag{15}$$

P_T：送信電力 [W]，A_e：有効開口面積，

G_t, G_r：送信，受信利得

ここで，P_{LOSS} は，送信アンテナから受信アンテナまでの間で吸収された電力であり，式 (15) と同様に計算することができる．また，雑音電力は熱雑音と端末内で加わる雑音を雑音係数 NF として式 (16) より算出した．

$$N = kBTN_F \tag{16}$$

k：ボルツマン定数，B：帯域幅，T:温度，N_F:ノイズ指数

2.7 変調方式

UWB の変調方式として，OOK(On-Off Keying)，及び BPSK(Binary Phase Shift Keying) を想定する．各変調方式のビット誤り率 (Bit Error Rate:BER) は，式 (17),(18) で求められる．

$$BER_{OOK} = \frac{1}{2}\mathrm{erfc}\sqrt{\frac{E_b}{4N_0}} \tag{17}$$

$$BER_{BPSK} = \frac{1}{2}\mathrm{erfc}\sqrt{\frac{E_b}{N_0}} \tag{18}$$

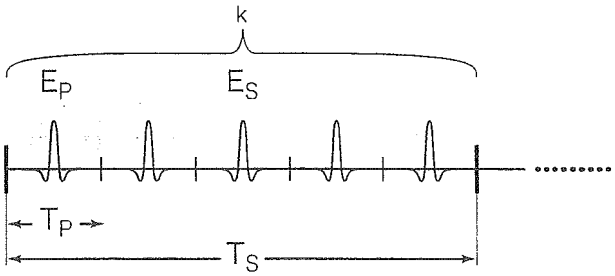

図 4　UWB 通信フレーム

UWB 通信フレームの構成を図 4 に示す．E_P は 1 パルスのもつエネルギー，E_S は 1 シンボルあたりのエネルギー，T_P はパルス間隔，T_S はシンボル長を表し，k は 1 シンボルを構成するパルス数である．E_b は情報 1 ビットあたりの信号エネルギーであり，N_0 は片側雑音電力密度である．1 シンボルあたりのエネルギーは $E_S = kE_P$ であるから，$E_b = E_S = kE_P$ となり，E_b/N_0 は式 (19) のように表せる．

$$\frac{E_b}{N_0} = k\frac{E_P}{N_0} \tag{19}$$

また，データ伝送レートを式 (20) のように定義する．

$$DataRate = \frac{1}{T_S} = \frac{1}{kT_P} \tag{20}$$

以上よりスループットを式 (21) のように定義し，評価に用いる．

$$\text{Throughput} = (1 - \text{BER}) \times DataRate \times D_c \tag{21}$$

3. 計算機シミュレーション

3.1 シミュレーション諸元

シミュレーション諸元を表 3.1 に示す．

3.2 シミュレーション結果

OOK，BPSK の各変調方式について，SNR に対するスループットの特性を評価した．BPSK 変調においては，熱エネルギー的に見ると情報ビットに関わらず kE_P だけのエネルギーを放射することになる．結果を図 5 に示す．

図 5 より，低 SNR 領域では SNR の上昇にあわせてスループットの向上が見られ，ある SNR を超えると熱影響によりス

表 2　シミュレーション共通諸元

媒質

構成	脂肪 (均一)
比熱 $c[J/kg \cdot ℃]$	2.3E+3
熱伝導率 $\kappa[W/m \cdot ℃]$	0.20
密度 $\rho[kg/m^3]$	0.94E+3
血液の密度 $\rho_b[kg/m^3]$	1.06E+3
血液の比熱 $c_b[J/kg \cdot ℃]$	3.9E+3
血液の温度 $T_b[℃]$	37.0
血液の流量率 $F[m^3/kg \cdot s]$	0.14E-6

媒質 Cole-Cole パラメータ

静誘電率 $\epsilon_s[F/m]$	9.8
誘電率 $(f = \infty)$ $\epsilon_\infty[F/m]$	2.5
誘電率 ϵ_1	3.0
誘電率 ϵ_2	15.0
誘電率 ϵ_3	3.30e+4
誘電率 ϵ_4	1.0e+7
緩和時間 τ_1	7.958e-12
緩和時間 τ_2	15.915e-9
緩和時間 τ_3	159.155e-6
緩和時間 τ_4	7.958e-3
係数 α_1	0.2
係数 α_2	0.1
係数 α_3	0.05
係数 α_4	0.01
静導電率 $\sigma_i[S/m]$	0.01

微小ダイポールアンテナ

長さ $dl[mm]$	10
半径 $dr[mm]$	2.0
送受信間距離 $d[mm]$	200
送信利得 Gt	1.5
受信利得 Gr	1.5

生体熱輸送方程式

初期体温 $T_0[℃]$	37.0
許容上昇温度 $T_{max}[℃]$	0.02
許容温度 $T_w[℃]$	0.01
解析空間 [mm]	100 × 100
セルサイズ (*)[mm]	0.5 × 0.5

(*) 安定条件を満たす

無線通信諸元

波形	1 階微分ガウシアンパルス
帯域幅 [GHz]	3
シンボル長 $T_S[nsec]$	25-200
パルス数 k	5
ノイズ係数 [dB]	20

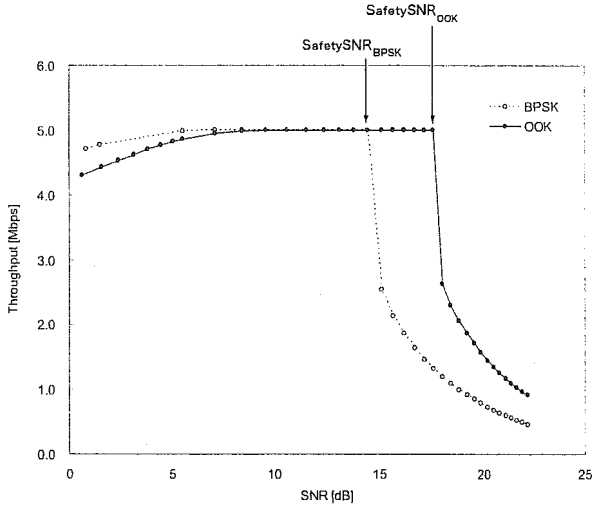

図 5　OOK,BPSK 変調の SNR 特性

ループットが急速に劣化しているのがわかる．図 5 において，スループットが最大となる SNR 領域の存在は，熱影響による侵襲性を十分に抑えつつ，通信を行えることを意味している．ここで熱影響及び，通信品質の劣化によるスループットの低下が見られない最大 SNR を $Safety$SNR と定義する．このとき，各変調方式において，

$$Safety\mathrm{SNR}_{\mathrm{OOK}} = 17.6[dB]$$
$$Safety\mathrm{SNR}_{\mathrm{BPSK}} = 14.5[dB]$$

となり，OOK 変調が BPSK 変調に比べて約 3dB 高い送信電力を確保できることがわかる．

OOK 変調方式では，情報ビットの"0","1"をそれぞれ 0, $k\sqrt{E_P}$ として変調し，伝送される．そのため，情報に含まれる"1"の割合を減らすことで，低消費電力，低熱侵襲が実現できると考えられる．情報ビットに含まれる"1"の割合を α とし，各データ伝送レートに対するスループットの評価を行った．結果を図 6 に示す．

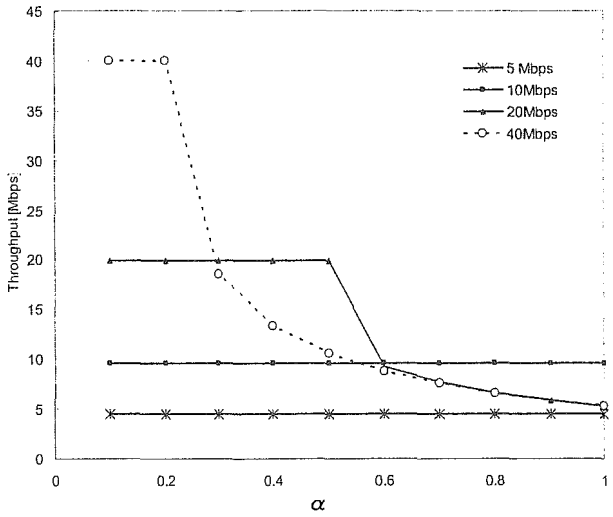

図 6　OOK 変調の α によるスループット特性

図 6 において，データ伝送レートをあげることはパルス間隔 T_P を狭めることを意味し，送信電力は増加する．これによって伝送レート 10[Mbps] までは α に限らずスループットに大幅な劣化は見られない．それに対し，データ伝送レート 20[Mbps] 以上では α の値により，劣化が見られる．これは情報ビット中の"1"の分布が熱影響に大きな影響を与えることを意味する．このため，高速伝送時は系列変調等によって情報ビットに含まれる"1"の数を減らすことにより熱影響を抑えられると考えられる．

4. むすび

本稿では，生体内での無線通信方式の評価，検討のためのモデルを提案した．このモデルでは，安全上昇温度を設定することにより，微小ダイポールアンテナから送信された信号の熱影響からデューティーサイクルを算出し，スループットに反映させることで両方を考慮した議論を可能にした．このモデルに基づき，OOK，BPSK の各変調方式に関して評価した結果，OOK 変調が生体内通信に適していることを示した．今後，より実際に近いモデルを考えるために，雑音電力や送受信機の発熱に関して考慮する必要があり，実験による確認も必要であると考えられる．

文　献

[1] 大森 豊明 "バイオ電磁工学とその応用" 株式会社フジ・テクノシステム pp.-(1992)

[2] ICNRP,"GUIDLINES FOR LIMITING EXPOSURE TO TIME-VARYING ELECTRIC,MAGNETIC,AND ELECTROMAGNETIC FIELDS(up to 300GHz)"

[3] 総務省,"電波防護指針 諮問第 89 号「電波利用における人体防護の在り方」(平成 9 年) "

[4] 加藤博和, 齊藤一幸, "人体の熱定数と血流に関する数値例", 人体電磁ファントム研究会

[5] Y. Prakash, S. Lalwani, S. K. S. Gupta, E. Elsharawy, and L. Schwiebert, "Towards a propagation model for wireless biomedical applications" ,IEEE ICC 2003, vol.3, pp.1993-1997, May 2003

[6] K. S. Cole and R. H. Cole, "Dispersion and absorption in dielectrics : 1. Alternating current characteristics.," *Journal of Chemical Physics*, Apr. 1941.

[7] Camelia Gabriel, Sami Gabriel, "MSc.COMPILATION OF THE DIELECTRIC PROPERTIES OF BODY TISSUES AT RF AND MICROWAVE FREQUENCIES", http://niremf.ifac.cnr.it/docs/DIELECTRIC

PAPER Special Section on Adaptive Signal Processing and Its Applications

Maximum Likelihood Estimation of Trellis Encoder and Modulator Transition Utilizing HMM for Adaptive Channel Coding and Modulation Technique

Kentaro IKEMOTO[†a)], *Student Member and* Ryuji KOHNO[†b)], *Fellow*

SUMMARY In order to achieve adaptive channel coding and adaptive modulation, the main causes of degradation to system performance are the decoder selection error and modulator estimation error. The utilization of supplementary information, in an estimation system utilizing channel estimation results, blind modulation estimation, and blind encoder estimation using several decoders information and encoder transitions have been considered to overcome these two problems. There are however many issues in these methods, such as the channel estimation difference between transmitter and receiver, computational complexity and the assumption of perfect Channel State Information (CSI). Our proposal, on the other hand, decreases decoder and demodulator selection error using a Hidden-Markov Model (HMM). In order to estimate the switching patterns of the encoder and modulator, our proposed system selects the maximum likelihood encoder and modulator transition patterns using both encoder and modulator transition probability based on the HMM obtained by CSI and also Decoder and Demodulator Selection Error probabilities. Therefore, the decoder and demodulation results can be achieved efficiently without any restraint on the pattern of switching encoder and modulation.

key words: *hidden-Markov model, maximum likelihood encoder and modulator transition, decoder and demodulator selection error*

1. Introduction

Recently, there has been a growing amount of research into mobile communications, especially adaptive algorithms that can achieve optimal system constructions considering time and/or geographic environmental problems as well as an adaptive algorithm that adjusts the constructions in order to satisfy users needs. One of the research topics, which has attracted much attention, is adaptive channel coding and the adaptive modulation scheme [1]. The aim of this research is to alter encoders or modulators in order to achieve the desired performance.

On the other hand, to change the encoders and modulators, it is necessary to design a pattern for transmitter and receiver. Therefore, along with the problem that poor decoding performance occurs due to error in selection of decoders and demodulators, the sequence synchronization problem that occurs due to the utilization of several decoders with different coding rates or different modulation orders is also a crucial problem.

Manuscript received June 25, 2004.
Manuscript revised October 4, 2004.
Final manuscript received November 16, 2004.

[†]The authors are with the Graduate School of Engineering, Yokohama National University, Yokohama-shi, 240-8501 Japan.
a) E-mail: ikemoto@kohnolab.dnj.ynu.ac.jp
b) E-mail: kohno@ynu.ac.jp

DOI: 10.1093/ietfec/e88–a.3.669

In order to solve these problems, there are two main methods [2]–[6]. One is to add supplemental information at the transmitter to indicate which encoder and modulation scheme are being used, the other is to estimate which encoder and modulation scheme are used at the receiver using the decoder and demodulator results. In the first case, in order to prevent error in the supplementary information, error correction codes with high quality are needed. However, longer redundancy causes lower transmission rates, and this rate becomes even lower when the encoder and modulator are changed frequently. Additionally, one can consider using pilot symbols to choose encoder and modulator, however, this method requires perfect channel estimation, or a non appropriate decoder and demodulator can be selected. On the other hand, in the latter case, the minimum distance between encoders determines encoder estimation accuracy. Just as with the minimum distance between codewords, the longer the distance, the better the performance. Due to the limited choices of encoder, it is hard to change the estimation accuracy adaptively. Moreover, modulation estimation accuracy depends on the distance between any two of the constellation points.

In addition, the encoding method considering a finite state machine utilizing the fading channel model has also been studied [7]. However, this method cannot accommodate all the channel models. It means that it is not clear whether the proposed method of limiting the encoder transition by FSM is appropriate to support estimation of dynamic channels. To solve this problem, Ref. [7] extended the layered encoder transition scheme which selects several encoder transitions of FSMs that can adapt to changes in the channel condition. However this method is not realistic because this has to predict a change of channel condition over a long period to select the optimum encoder switching several FSMs, each with different encoder transitions. In order to solve this problem, we focus on the HMM. Our proposal can adapt to changes in the channel condition and also select the optimum encoder and modulator by using prediction of channel condition in switching timing. Fading channel-modeling schemes using HMM have been recently widely studied [8], [9] which can accurately model the fading channel and also estimate the parameters of HMM by using the Baum-Welch algorithm for a time varying channel. We propose a scheme using this kind of channel modeling to encode and modulate. Our proposals performance deteriorates

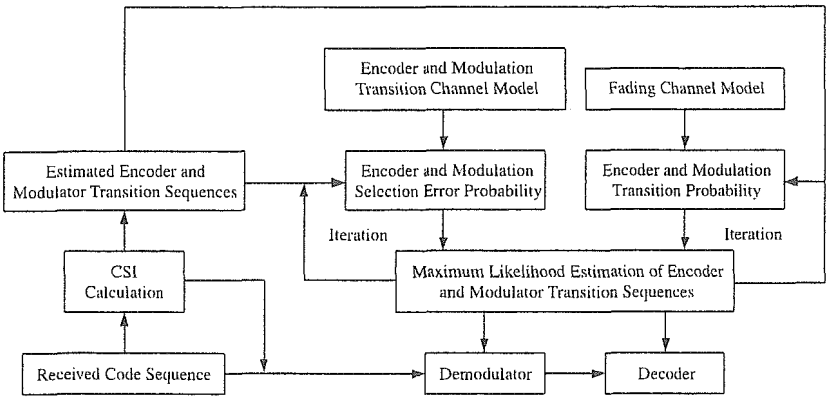

Fig. 1 System model.

when the channel estimations at transmitter and receiver are different, or if the estimation of encoder and modulator at the receiver is invalid. Consequently, we additionally add an algorithm to our proposal to reduce decoder and demodulator selection errors using the HMM.

In more detail, our proposed system selects the maximum likelihood encoder and modulator transition by using both encoder and modulator transition probabilities, based on the HMM obtained using CSI and Decoder and Demodulator Selection Error probabilities. We use the Expectation-Maximization (EM) algorithm [10] as a maximum likelihood algorithm, and this proposal can be realistically achieved with reasonable computational complexity relying only on the number of trellis states, which differs from the conventional system. Compared with a conventional finite state machine scheme whose transition pattern and encoder or modulator switching pattern have a one to one correspondence, the proposed HMM scheme whose transition pattern is probabilistically determined is more efficient in a fading channel. Therefore, the decoder and demodulation results can be achieved efficiently without any restraint on the pattern of encoder and modulator switching.

This paper is organized as follows. In Sect. 2, considering our proposed adaptive coding and modulation scheme under HMM, we show the encoder and modulator switching estimation schemes with maximum likelihood in more detail. In Sect. 3, the performance of the proposed system using computer simulations is shown. Finally, we conclude this paper in Sect. 4.

2. Adaptive Coding and Modulation Scheme Using HMM

2.1 System Model

The transmit sequence is shown in Fig. 2. We assume a TDD system with L frames, and each frame consists of d transmit bits plus p pilot symbols for channel estimation. According to the channel estimation result, the appropriate encoder and modulator are selected for the information sequence. Notice that the channel model is HMM. Figure 1 shows the proposed system block diagram. Figure 3 shows the flowchart of our proposed system.

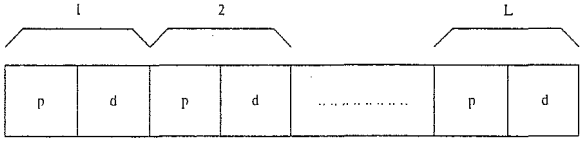

Fig. 2 Frame structure of received data for fading channel.

In Fig. 3, we assume a fading channel with Rayleigh-distributed amplitude fading and no phase coherence, which is equivalent to independent Gaussian amplitude fading on both the in-phase and quadrature components of the transmitted symbols. We use the EM-based receiver [11] to obtain the optimum sequence estimation and channel parameters to estimate encoder and modulator. The EM algorithm is a broadly applicable approach to the iterative computation of maximum likelihood estimates, useful in a variety of incomplete-data problems [12], [13]. On each iteration of the EM algorithm, there are two steps called the expectation step (E-step) and the maximization step (M-step). One of the reasons for its attractiveness is that it provides a numerical method for obtaining maximum likelihood estimates that might not be readily available otherwise. For the sequence estimation problem studied in this paper, the algorithm converges surprisingly quickly and has an efficient implementation that makes it of practical as well as theoretical interest.

Figure 2 illustrates the received data for $T = p + d$ and $U = pL$. In setting the initial fading estimate, the algorithm uses the fact that the symbols in positions $1, (T+1), \cdots, (U-1)T + 1$ are known. An initial fading estimate is then easily obtained by summing the data in each of the U known bit positions and dividing by U.

$$a_0 = \frac{1}{U} \sum_{k=0}^{U-1} r_{kT+1}. \tag{1}$$

Further, the maximization step of the algorithm needs only be performed over the $U(T-1)$ modulated bits, and since these bits are randomly chosen, maximizing over the set of length $U(T-1)$ bit sequences is equivalent to making

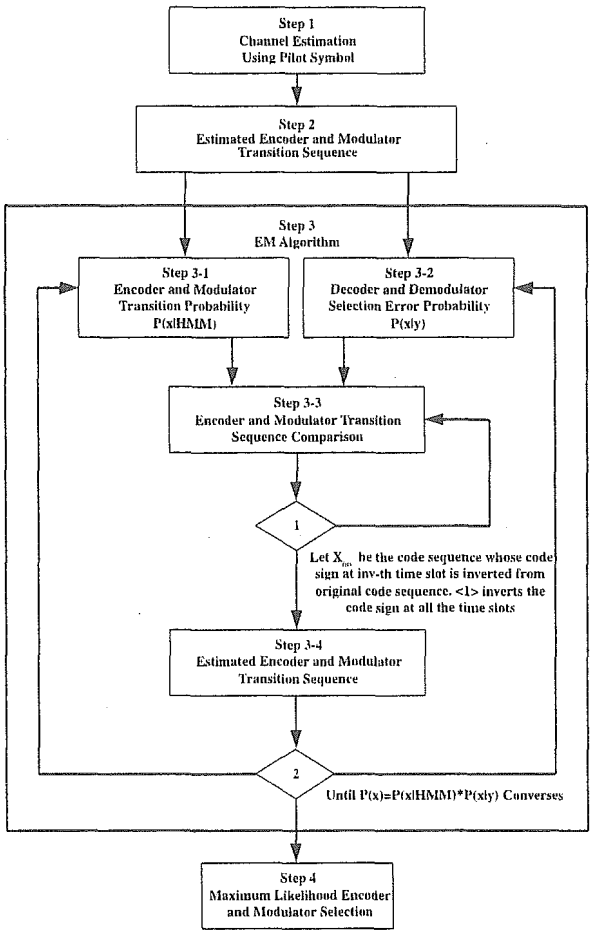

Fig. 3 Flowchart of our proposed system.

symbol-by-symbol decisions on each bit. Seq^{i+1} is the sequence where components are easily obtained through

$$Seq_k^{i+1} = sgn[\Re(r_k^{\dagger} a_i)] \tag{2}$$

where $sgn(\cdot)$ is the signum function, i is number of iteration and $\dagger$ denotes conjugated transpose. For the nonbinary case, the above symbol-by-symbol estimator is replaced by

$$Seq_k^{i+1} = \arg\max_{Seq_k} \Re(r_k^{\dagger} Seq_k a_i). \tag{3}$$

After estimating the channel with the p received pilot symbols in Step 1, the result is used to estimate the encoder and modulator as well as the received sequence compensation. The encoder and modulator can be selected to meet performance with lower than desired BER depending on the change in estimated SNR by using Seq in (3) which is obtained by EM algorithm receiver. With the selected encoder and modulator in Step 2, the encoder and modulator switching pattern is constructed to obtain a switching pattern probability using the BCJR algorithm in Step 3-1. Additionally, the probability of decoder and demodulator selection errors is extracted using CSI and selected encoder and modulator in Step 3-2. With these two probabilities, iterative maximum likelihood estimation is implemented to find a more appropriate encoder and modulator switching pattern in Step 3-3 and 3-4.

2.2 Definition of Maximum Likelihood Estimation of Encoder and Modulator Switching Patterns

This section describes how to define the maximum likelihood encoder and modulator selection, Step 4. When HMM is used as a probabilistic model for the encoder and modulator switching pattern, this model has the possibility to derive the conditional probability $P(\hat{x}|HMM)$ (Step 3-1) using the BCJR algorithm, where $\hat{x} = (x_1, x_2, \cdots, x_t, \cdots x_{time})$ represents the switching pattern sequence. Defining $P(\hat{x}|\hat{y})$ (Step 3-2) as the conditional probability that the estimated switching pattern $\hat{y}$ at the receiver provides a value close to $\hat{x}$, $P(\hat{x}|\hat{y})$ can be derived from CSI or decoder and demodulator selection errors based on the selected encoder and modulator. Moreover, to find the optimum sequence $\hat{x}$ from both of these probabilities leads to a maximum likelihood estimation of the encoder and modulator switching pattern.

2.3 Extraction of the Probability of Encoder and Modulator Switching Pattern

The conditional probability $P(\hat{x}|HMM)$ of encoder and modulator switching pattern sequence $\hat{x}$ when using the HMM can be easily derived by the BCJR algorithm due to the utilization of the HMM model. Notice that we use the normalized BCJR algorithm that considers the underflow problem. Let us define the forward metric as $\alpha_t(s)$, and the backward metric as $\beta_t(s)$, where $t = (1, 2, \cdots, time)$. Assume the channel condition is the same as the HMM, the transition probability from state s to state $\acute{s}$ is $p_{s\acute{s}}$, and according to this transition, $p_{s\acute{s}}(x_t)$ represents the probability when selected encoder and modulator pattern is transformed to be a code x_t. Note that there are N_s states, where N=$(1, \cdots, s, \acute{s}, \cdots, N_s)$. $\alpha_t(s)$ and $\beta_t(s)$ are given by (4) and (5), and calculated recursively.

$$\alpha_t(\acute{s}) = \sum_{s=1}^{N_s} \alpha_{t-1}(s) p_{s\acute{s}} p_{s\acute{s}}(x_t) \tag{4}$$

$$\beta_t(\acute{s}) = \sum_{s=1}^{N_s} \beta_{t+1}(s) p_{s\acute{s}} p_{s\acute{s}}(x_{t+1}) \tag{5}$$

The initial values are $\alpha_1(N) = (\pi_1, \pi_2, \cdots, \pi_{N_s})$, where $\sum_{s=1}^{N_s} \pi_s = 1$ and $\beta_{time}(N) = 1$, respectively, and due to the necessity of normalization, (6) and (7) are used.

$$\bar{\alpha}_t(\acute{s}) = \frac{1}{\sum_{\acute{s}=1}^{N_s} \alpha_t(\acute{s})} \alpha_t(\acute{s}) \tag{6}$$

$$\bar{\beta}_t(\acute{s}) = \frac{1}{\sum_{\acute{s}=1}^{N_s} \beta_t(\acute{s})} \beta_t(\acute{s}) \tag{7}$$

Then $P(\hat{x}|HMM)$ is given by (8).

$$P(\hat{x}|HMM) = \sum_{s=1}^{N_s} \alpha_{t-1}(s) \cdot \sum_{\acute{s}=1}^{N_s} \beta_t(s) \cdot \sum_{s=1}^{N_s} \sum_{\acute{s}=1}^{N_s} \bar{\alpha}_{t-1}(s) p_{s\acute{s}} p_{s\acute{s}}(x_t) \bar{\beta}_t(\acute{s}) \quad (8)$$

2.4 Extraction of Decoder and Demodulator Selection Error Probability

Define $P(\hat{x}|\hat{y})$ as the probability of sequence $\hat{x}$ when the received encoder and modulator switching pattern sequence is $\hat{y}$. $P(\hat{x}|\hat{y})$ belongs to a binary symmetric channel, and given by,

$$P(\hat{x}|\hat{y}) = p^d(1-p)^{n-d} \quad (9)$$

where p represents the decoder or demodulator selection error, d is the number of these errors and also can be described as the hamming distance between $\hat{x}$ and $\hat{y}$. n is the length of encoder and modulator switching pattern sequence.

2.5 Maximum Likelihood Estimation Scheme for Encoder and Modulator Selection

We focus our attention on seeking a sequence $\hat{x}$ that maximizes both $P(\hat{x}|HMM)$ and $P(\hat{x}|\hat{y})$. We adopt the EM algorithm for our proposal. Step 3 in Fig. 3 indicates this algorithm. Define $\hat{x}^i = (x_1^i, x_2^i, \cdots, x_t^i, \cdots, x_{time}^i)$ as the sequence of estimated encoder or modulator switching pattern in i-th iteration. In the E-step, $P(\bar{x}_{inv}^i)$ is derived by multiplying $P(\bar{x}_{inv}^i|HMM)$ by $P(\bar{x}_{inv}^i|\hat{y})$. Let $\bar{x}_{inv}^i$ $(inv = 1, \cdots, time)$ be the code sequence whose code sign at inv-th time slot is inverted from the original code sequence constructed from encoder and modulator, and substitute this into (10) to obtain t sequences and thus t probabilities of $P(\bar{x}_{inv}^i)$. In the M-step, each of the t probabilities, $P(\bar{x}_{inv}^i)$, is compared to the original sequence $P(\hat{x}^i)$, and we invert the code sign at all the time slots whose probability $P(\bar{x}_{inv}^i)$ is larger than the original sequence probability $P(\hat{x}^i)$, thus obtain one sequence $P(\hat{x}^{i+1})$. (11) indicates the M-step algorithm, where T represents the transpose. In the next iteration, $P(\bar{x}_{inv}^{i+1}|HMM)$ and $P(\bar{x}_{inv}^{i+1}|\hat{y})$ are extracted again using (8) and (9), and then substituted into (10) and (11). After several iterations the convergence of $P(\hat{x}^{i+1})$, $\hat{x}^{i+1}$ is considered to be the maximum likelihood encoder and modulator selections.

$$P(\bar{x}_{inv}^i) = P(\bar{x}_{inv}^i|HMM) \cdot P(\bar{x}_{inv}^i|\hat{y}) \quad (10)$$

$$P(\hat{x}^{i+1}) = (P(x_1^{i+1}), P(x_2^{i+1}), \cdots, P(x_{time}^{i+1})) = \begin{pmatrix} \arg\max(P(\bar{x}_1^i), P(\hat{x}^i)), \\ \arg\max(P(\bar{x}_2^i), P(\hat{x}^i)), \\ \vdots \\ \arg\max(P(\bar{x}_{inv}^i), P(\hat{x}^i)) \end{pmatrix}^T \quad (11)$$

3. Computer Evaluation

We show the reduction of decoder and demodulator selection errors in order to clarify the effectiveness of our proposal.

3.1 Prerequisite

Assuming that the fading channels are defined by HMM, and AWGN channels. The transition probability $p_{s\acute{s}}$ from state s to $\acute{s}$, and the probability $p_{s\acute{s}}(x_t)$ that $p_{s\acute{s}}$ transforms the encoder and modulator selected based on this probability to x_t, are considered to be given. Moreover, the synchronization at the receiver is considered to be perfect. The information data is encoded by the encoder selected based on CSI information obtained by EM based receiver, and the encoded data $a_i(i = 1, 2, \cdots, n)$ is obtained. Notice that the code lengths are the same even if the code rates or the error correction probabilities are different. The same number of symbols is transmitted for any modulation scheme in each packet. The timing for switching the modulation scheme is determined by synchronizing the packet length of BPSK. Therefore, the modulation scheme is switched by the length of packet which is one frame with BPSK, two frames with QPSK, three frames with 8PSK, and four frames with 16QAM.

3.2 Evaluation of Reduction of Selection Errors

Table 1 shows the simulation parameters. The fading channels rely on the HMM, and the state of the HMM is 2. Figure 4 shows the trellis diagram and state transition of HMM. The probability $p_{s\acute{s}}$ and $p_{s\acute{s}}(x_t)$, and the code sequence x_t are described in the previous subsection and are defined as in Table 2. We describe CM1, CM2, CM3 and CM4 as quasi-static fading channel models whose characteristics are different to each other. These channel models still stay constant over more than two packets. In CM1, channel state changes slowly, therefore the system selects the same modulator for long term. On the other hand, in CM2, channel state changes faster than CM1; therefore, channel condition changes randomly compared to CM1. CM3 is defined as a bad channel condition where system almost always transmits with BPSK. In CM4, channel condition between sate s and $\acute{s}$ is defined to almost be the same and each channel selects the almost same number of modulations between BPSK and QPSK randomly. These channel models cover

Table 1 Simulation parameters.

Information Length	50
Codeword Length	100
Coding Rate	0.5
Pilot Symbol	10
Modulation	BPSK QPSK
Frame Length	110 (BPSK) 55 (QPSK)
Packet Length	110 Symbols
Encoder and Modulator Switching Sequence Length	25 49, 100
Iteration of EM	1-6